

# BTeV - an Experiment to Measure Mixing, CP Violation and Rare Decays of Beauty and Charm at the Fermilab Collider<sup>1</sup>

## Abstract

We discuss the physics goals and rationale for a detector to study Beauty and Charm decays in the forward direction at the Fermilab Tevatron. We then describe the BTeV detector which has been designed to achieve these goals and present its physics reach based on extensive simulation. We conclude by comparing BTeV to other experiments designed to explore similar topics.

## The BTeV Collaboration

- A. Kulyavtsev, M. Procaro<sup>2</sup>, J. Russ, and J. You  
Carnegie Mellon University, Pittsburgh, PA 15213, USA
- J. Cumalat, University of Colorado, CO 80309, USA
- J. A. Appel, C. N. Brown, J. Butler, H. Cheung, D. Christian, G. Chiodini,  
S. Cihangir, I. Gaines, P. Garbincius, L. Garren, E. E. Gottschalk,  
G. Jackson, P. Kasper, P. H. Kasper, R. Kutschke, S. W. Kwan, P. Lebrun,  
P. McBride, L. Stutte, and J. Yarba, Fermilab, Batavia, IL 60510, USA
- P. Avery, and M. Lohner, University of Florida, Gainesville, FL 32611, USA
- R. A. Burnstein, D. M. Kaplan, L. M. Lederman, H. A. Rubin, and C. White  
Illinois Institute of Technology, Chicago, IL 60616, USA
- D. Kim, M. Selen, and J. Wiss, University of Illinois at Urbana-Champaign,  
IL 61801-3080, USA
- R. W. Gardner and D. R. Rust, Indiana University, Bloomington, Indiana, 47405, USA
- E. Casimiro, D. Menasce, L. Moroni, D. Pedrini, and S. Sala  
INFN and University of Milano, Italy
- G. Boca, G. Liguori, and P. Torre, Dipartimento di Fisica Nucleare e Teorica,  
Universita' di Pavia and INFN, Sez. di Pavia, Italy
- A. A. Derevschikov, Y. M. Goncharenko, V. Yu. Khodyrev, A. P. Meschanin,  
L. V. Nogach, K. E. Shestermanov, L. F. Soloviev, and A. N. Vasiliev  
Institute of High Energy Physics (IHEP), Protvino, Moscow Region, Russia
- C. Newsom, The University of Iowa, Iowa City, IA 52242-1479
- Y. Kubota, R. Poling, A. Smith and B. Speakman, University of Minnesota  
MN 55455, USA
- T. Y. Chen, Nanjing University, Nanjing 210008, China
- V. Papavassiliou, New Mexico State University

---

<sup>1</sup>Submitted to the XXXth International Conference on High Energy Physics, July 27 - August 2, 2000, Osaka, Japan

K. Honscheid, and H. Kagan, Ohio State University, Columbus, OH 43210, USA  
W. Selove, University of Pennsylvania, Philadelphia, PA 19104, USA  
A. Lopez , University of Puerto Rico, Mayaguez, Puerto Rico  
T. Coan, Southern Methodist University, Dallas, TX 75275, USA  
M. Alam, State University of New York at Albany, Albany, NY 12222, USA  
X. Q. Yu, University of Science and Technology of China,  
Joint Institute for High Energy Physics, Hefei, Anhui 230027, China  
M. He, Shandong University, Jinan, Shandong 250100, China  
S. Shapiro (emeritus), Stanford Linear Accelerator Center, PO Box 4349,  
Stanford, CA 94309, USA  
M. Artuso, G. Majumder, R. Mountain, T. Skwarnicki, S. Stone, J. C. Wang, and A. Wolf  
Syracuse University, Syracuse, NY 13244-1130, USA  
K. Cho, T. Handler and R. Mitchell, University of Tennessee  
Knoxville, TN 37996-1200, USA  
A. Napier, Tufts University, Medford, MA 02155, USA  
D. D. Koetke, Valparaiso University, Valparaiso, IN 46383, USA  
W. Johns, P. Sheldon, K. Stenson, and M. Webster, Vanderbilt University,  
Nashville, TN 37235, USA  
M. Sheaff, University of Wisconsin, Madison, WI 53706, USA  
J. Slaughter, Yale University, High Energy Physics, New Haven, CT 06511, USA  
S. Menary, York University, ON M3J 1P3, Canada

# 1 Motivation

BTeV is a program designed to challenge the Standard Model explanation of CP Violation, mixing and rare decays in the  $b$  and  $c$  quark systems. Exploiting the large number of  $b$ 's and  $c$ 's produced at the Tevatron collider, we will make precise measurements of Standard Model parameters and an exhaustive search for physics beyond the Standard Model.

BTeV can perform the compelling physics studies that need to be done, and is not limited by current constraints on what studies can be done. We are not constrained by a central geometry that is prescribed to study high  $p_t$  physics, nor are we limited by relatively low numbers of  $b$ -flavored hadrons as in  $e^+e^-$  colliders. BTeV excels in several crucial areas including: triggering on decays with purely hadronic final states, charged particle identification, electromagnetic calorimetry and proper time resolution.

In the Standard Model, CP violation has its origin in the phenomenon of quark mixing. As a result, the Standard Model makes very specific connections among various kinds of CP violating  $B$  decays and among  $B$  decays, kaon and charm decays. Standard Model quark mixing is described by the Cabibbo-Kobayashi-Maskawa matrix [1],

$$\begin{pmatrix} d' \\ s' \\ b' \end{pmatrix} = \begin{pmatrix} V_{ud} & V_{us} & V_{ub} \\ V_{cd} & V_{cs} & V_{cb} \\ V_{td} & V_{ts} & V_{tb} \end{pmatrix} \begin{pmatrix} d \\ s \\ b \end{pmatrix} . \quad (1)$$

The unprimed states are the mass eigenstates, while the primed states denote the weak eigenstates. The  $V_{ij}$ 's are complex numbers that can be represented by four independent real quantities, if the matrix is unitary. These numbers are fundamental constants of nature that need to be determined from experiment, as with any other fundamental constant such as  $\alpha$  or  $G$ . Measuring them accurately is important, but the most important goal of BTeV is to make a broad range of measurements to check whether the whole picture is correct. If inconsistencies appear, that means there is new physics in play, physics beyond the Standard Model. More detailed study would then elucidate the nature of this new physics.

To confront the Standard Model, measurements are necessary on CP violation in  $B^0$  and  $B_s$  mesons,  $B_s$  mixing, rare  $b$  decay rates, and on mixing, CP violation and rare decays in the charm sector.

Although much has been learned about  $b$  and  $c$  decays from past and current experiments, and more will be learned soon; many, if not most, of the crucial measurements will not have been made by the dawn of the LHC era. It is just as important to see if the "Standard Model" explains quark mixing and CP violation as it is to see if there is a "Standard Model" Higgs particle which generates mass.

With BTeV, we can mount a formidable assault on the CKM explanation of CP violation and mixing. Simply stated, we must do this physics!

## 2 Physics Goals

BTeV is designed to make a complete enough set of measurements on the decays of hadrons containing  $b$  and  $c$  quarks so as to be able to either accurately determine Standard Model parameters or to discover fundamental inconsistencies that could lead us to an understanding beyond the model. The most important measurements to make involve mixing, CP violation and rare decays of hadrons containing  $b$  or  $c$  quarks.

Using unitarity, Aleksan, Kayser and London [2] have shown that the CKM matrix can be expressed in terms of four independent phases. These are taken as:

$$\begin{aligned} \beta &= \arg\left(-\frac{V_{tb}V_{td}^*}{V_{cb}V_{cd}^*}\right), & \gamma &= \arg\left(-\frac{V_{ub}^*V_{ud}}{V_{cb}^*V_{cd}}\right), \\ \chi &= \arg\left(-\frac{V_{cs}^*V_{cb}}{V_{ts}^*V_{tb}}\right), & \chi' &= \arg\left(-\frac{V_{ud}^*V_{us}}{V_{cd}^*V_{cs}}\right). \end{aligned} \quad (2)$$

Another phase  $\alpha$ , the angle between  $V_{ub}$  and  $V_{td}$ , is redundant with  $\beta$  and  $\gamma$ , since

$$\alpha + \beta + \gamma = \pi \quad . \quad (3)$$

It is important to uniquely measure all of these phases, including  $\alpha$ . CP asymmetry measurements often involve measuring  $\sin(2\phi)$ , where  $\phi$  is the angle of interest. When we measure  $\sin(2\phi)$  we have a four-fold ambiguity in  $\phi$ , namely  $\phi$ ,  $\pi/2 - \phi$ ,  $\phi + \pi$  and  $3\pi/2 - \phi$ . These ambiguities can mask the effects of new physics. One of our main tasks is to remove as many of the ambiguities as possible.

A complete program includes measuring the CP violating angles  $\alpha$ ,  $\beta$ ,  $\gamma$  and  $\chi$ , measuring the  $B_s$  oscillation frequency, searching for anomalous rates in “rare”  $b$  decays and searching for mixing and CP violation in the charm sector, where Standard Model rates are expected to be small and new physics could have large signals.

The “Physics Case,” presented in Chapter 1 of the proposal, describes in detail the measurements we wish to make and the specific decay modes that we envision using. Table 1 lists the most important physics quantities and suggested decay modes which measure them. We also list the detector characteristics needed to make each measurement. (Rare  $b$  decay measurements and charm physics are not included in this table.)

The BTeV detector, described below and in Chapter 2 of the proposal, possesses all of the properties required to carry out these measurements. Perhaps just as importantly, the detector is powerful enough to pursue physics in many areas of  $b$  and  $c$  production and decay. In the future, new final states that will be important to measure will surely emerge. BTeV, because of its excellent trigger, tracking, particle identification and photon detection, will be in prime position to investigate any such new ideas.

## 3 Rationale for a Forward Detector at the Tevatron

BTeV covers the forward direction, 10-300 mrad, with respect to both colliding beams. In Chapter 2 of the proposal we explain the reasons for this choice. We summarize them here.

Table 1: Required CKM measurements for  $B$  mesons and associated key detector characteristics.

Physics Quantity	Decay Mode	Hadron Trigger	$K\pi$ Sep	$\gamma$ Det	Decay Time $\sigma$
$\sin(2\alpha)$	$B^o \rightarrow \rho\pi \rightarrow \pi^+\pi^-\pi^o$	✓	✓	✓	
$\cos(2\alpha)$	$B^o \rightarrow \rho\pi \rightarrow \pi^+\pi^-\pi^o$	✓	✓	✓	
$\text{sign}(\sin(2\alpha))$	$B^o \rightarrow \rho\pi$ & $B^o \rightarrow \pi^+\pi^-$	✓	✓	✓	
$\sin(\gamma)$	$B_s \rightarrow D_s^\pm K^\mp$	✓	✓		✓
$\sin(\gamma)$	$B^- \rightarrow \overline{D}^0 K^-$	✓	✓		
$\sin(\gamma)$	$B^o \rightarrow \pi^+\pi^-$ & $B_s \rightarrow K^+K^-$	✓	✓		✓
$\sin(2\chi)$	$B_s \rightarrow J/\psi\eta', J/\psi\eta$			✓	✓
$\sin(2\beta)$	$B^o \rightarrow J/\psi K_S$				
$\cos(2\beta)$	$B^o \rightarrow J/\psi K^o, K^o \rightarrow \pi\ell\nu$				
$\cos(2\beta)$	$B^o \rightarrow J/\psi K^{*o}$ & $B_s \rightarrow J/\psi\phi$				✓
$x_s$	$B_s \rightarrow D_s^+\pi^-$	✓			✓
$\Delta\Gamma$ for $B_s$	$B_s \rightarrow J/\psi\eta', D_s^+\pi^-, K^+K^-$	✓	✓	✓	✓

Measured  $b\bar{b}$  cross-sections at the Tevatron integrate to  $100 \mu\text{b}$  [3]. One measurement by D0 in the forward region normalizes to  $180 \mu\text{b}$  [4]. Conservatively, we use the  $100 \mu\text{b}$  value for our physics projections. The yield of  $b$ -flavored hadrons then is  $\approx 4 \times 10^{11}$  in  $10^7$  seconds at a luminosity of  $2 \times 10^{32} \text{ cm}^{-2}\text{s}^{-1}$  and much of it is in the forward direction. The charm yield is approximately one order of magnitude higher and even more of it is concentrated in the forward direction.

According to QCD calculations of  $b$  quark production, there is a strong correlation between the  $B$  momentum and pseudorapidity,  $\eta$ . Shown in Fig. 1 is the  $\beta\gamma$  of the  $B$  hadron versus  $\eta$ , as computed by the Monte Carlo physics generator Pythia at  $\sqrt{s} = 2 \text{ TeV}$ . It can clearly be seen that near  $\eta$  of zero,  $\beta\gamma \approx 1$ , while at larger values of  $|\eta|$ ,  $\beta\gamma$  can easily reach values of 6. This is important because the mean decay length varies with  $\beta\gamma$  and, furthermore, the absolute momenta of the decay products are larger, allowing for a suppression of the multiple scattering error.

A crucially important correlation of  $b\bar{b}$  production at hadron colliders is shown in Fig. 2, where the production angle of the hadron containing the  $b$  quark is plotted versus the production angle of the hadron containing the  $\bar{b}$  quark. Here zero degrees represents the direction of the incident proton and 180 degrees, the incident antiproton. There is a very strong correlation in the proton or the antiproton directions: when the  $B$  is forward, the  $\bar{B}$  is also forward. (We call both the proton and antiproton directions forward.) This correlation between  $B$  and  $\bar{B}$  production is not present in the central region (near 90 degrees).

Thus, when a  $b$ -flavored hadron is produced forward, the accompanying  $\bar{b}$  is also produced in the forward direction, allowing for reasonable levels of flavor tagging. The large  $b$  quark yield, the long  $B$  decay length, the correlated acceptance for both  $b$ 's and the suppression of

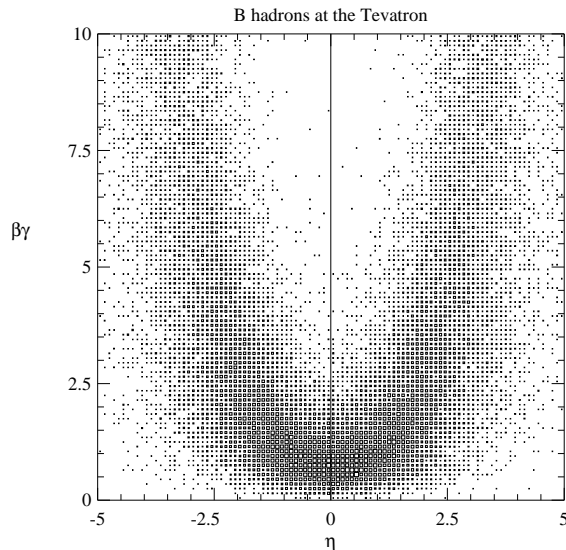


Figure 1:  $\beta\gamma$  of the  $B$  versus  $\eta$ .

multiple scattering errors due to the high  $b$  momenta, make the forward direction an ideal choice.

## 4 Detector Description

A sketch of the detector is shown in Fig. 3. The geometry is complementary to that used in current collider experiments. The detector looks similar to a fixed target experiment, but has two arms, one along the proton direction and the other along the antiproton direction.

The key design features of BTeV include:

- A dipole located on the IR, which gives BTeV an effective “two arm” acceptance;
- A precision vertex detector based on planar pixel arrays;
- A detached vertex trigger at Level 1 that makes BTeV efficient for most final states, including purely hadronic modes;
- Excellent particle identification using a Ring Imaging Cherenkov Detector (RICH);
- A high quality  $\text{PbWO}_4$  electromagnetic calorimeter capable of reconstructing final states with single photons,  $\pi^0$ 's,  $\eta$ 's or  $\eta'$ 's, and of identifying electrons;
- Precision tracking using straw tubes and silicon microstrip detectors, which provide excellent momentum and mass resolution;
- Excellent identification of muons using a dedicated detector with the ability to supply a dimuon trigger; and

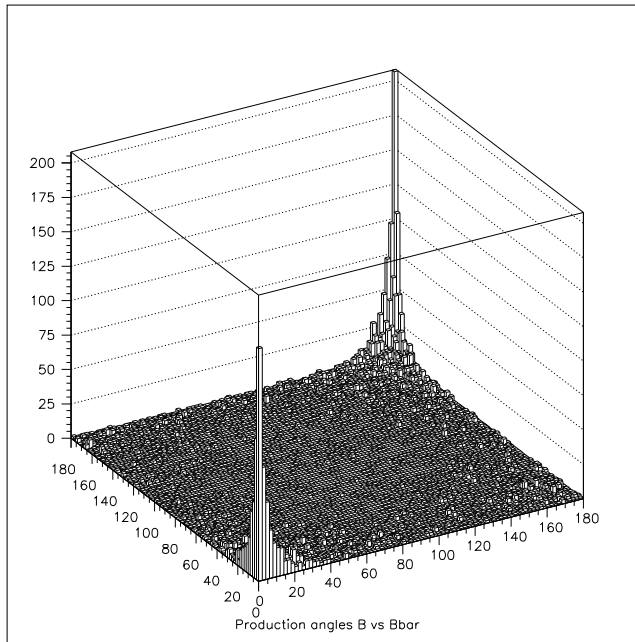


Figure 2: The production angle (in degrees) for the hadron containing a  $b$  quark plotted versus the production angle for a hadron containing a  $\bar{b}$  quark, from the Pythia Monte Carlo generator.

- A very high speed and high throughput data acquisition system which eliminates the need to tune the experiment to specific final states.

Each of these key elements of the detector is discussed in Part 2 of the proposal. Here we discuss them briefly.

#### 4.1 Dipole Centered on the Interaction Region

A large dipole magnet, with a 1.6 T central field, is centered on the interaction region. In addition to giving us a compact way of providing momentum measurements in both “forward” directions, it provides magnetic deflection in the vertex detector, which is exploited by the trigger to remove low momentum tracks, which could have been deflected by multiple Coulomb scattering, from its search for detached tracks.

#### 4.2 The Pixel Vertex Detector

In the center of the magnet there is a silicon pixel vertex detector. This detector serves two functions: it is an integral part of the charged particle tracking system, providing accurate vertex information for the offline analysis; and it delivers very clean, precision space points to the BTeV vertex trigger.

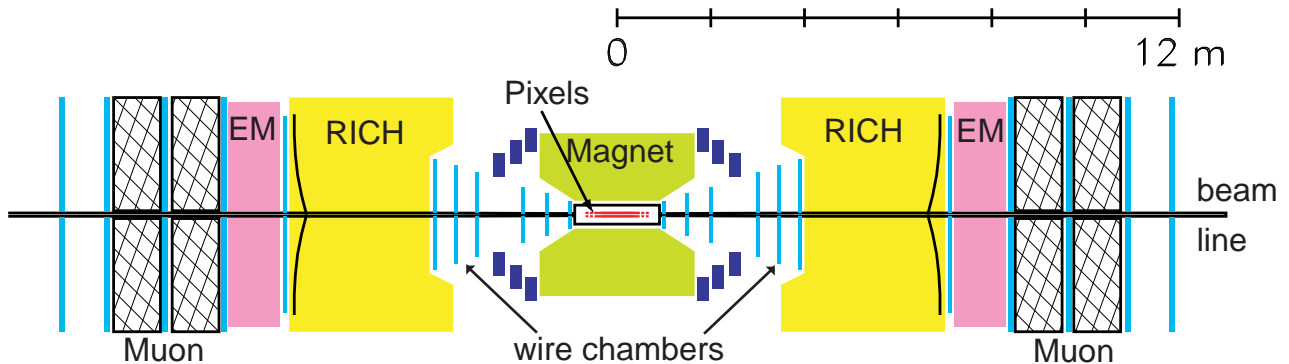


Figure 3: A sketch of the BTeV detector. The two arms are identical.

We have tested prototype pixel devices in a beam at Fermilab. These consist of  $50 \mu\text{m} \times 400 \mu\text{m}$  pixels bump-bonded to custom made electronics chips developed at Fermilab. A comparison of the position resolution achieved in the test beam and the Monte Carlo simulation is shown in Fig. 4. The resolution is excellent and exceeds our requirement of  $9 \mu\text{m}$ .

The critical quantity for a  $b$  experiment is  $L/\sigma_L$ , where  $L$  is the distance between the primary (interaction) vertex and the secondary (decay) vertex, and  $\sigma_L$  is its error. For central detectors the  $B$ 's are slower, because the mean transverse  $B$  momentum is  $5.3 \text{ GeV}/c$ , virtually independent of the longitudinal momentum. Since they also suffer more multiple scattering, they have relatively poorer  $L/\sigma_L$  distributions. LHC-b, on the other hand, does not benefit by going to higher momentum because, after a momentum of around  $10 \text{ GeV}/c$  (depending on the detector),  $\sigma_L$  also increases linearly.

The efficacy of this geometry is illustrated by considering the distribution of the resolution on the  $B$  decay length,  $L$ , for the decay  $B^0 \rightarrow \pi^+\pi^-$ . Fig. 5 shows the r.m.s. errors in the decay length as a function of momentum; it also shows the momentum distribution of the  $B$ 's accepted by BTeV. The following features are noteworthy:

- The  $B$ 's used by BTeV peak at  $p = 30 \text{ GeV}/c$  and average about  $40 \text{ GeV}/c$ .
- The decay length is equal to  $450 \mu\text{m} \times p/M_B$ .
- The error on the decay length is smallest near the peak of our accepted momentum distribution. It increases at lower values of  $p$ , due to multiple scattering, and increases at larger values of  $p$  due to the smaller angles of the Lorentz-boosted decay products.

### 4.3 The Detached Vertex Trigger

It is impossible to record data from each of the 7.5 million beam crossings per second. A prompt decision, colloquially called a “trigger,” must be made to record or discard the data from each crossing. The main BTeV trigger is provided by the silicon pixel detector. The Level 1 Vertex Trigger inspects every beam crossing and, using only data from the pixel



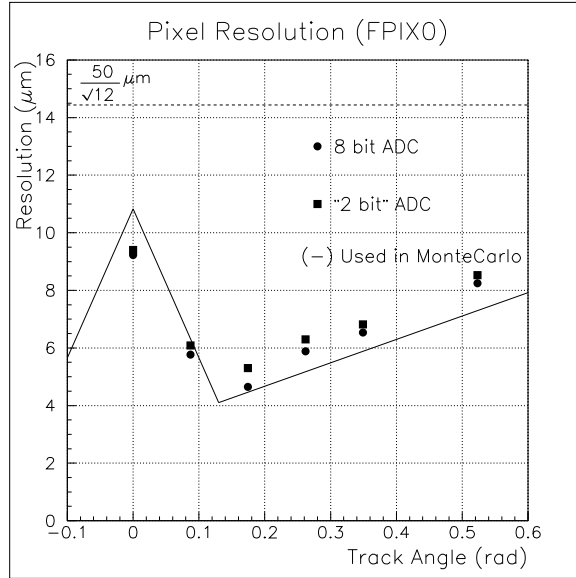


Figure 4: The resolution achieved in our test beam run using 50  $\mu\text{m}$  wide pixels and an 8-bit ADC (circles) or a 2-bit ADC (squares), compared with our simulation (line).

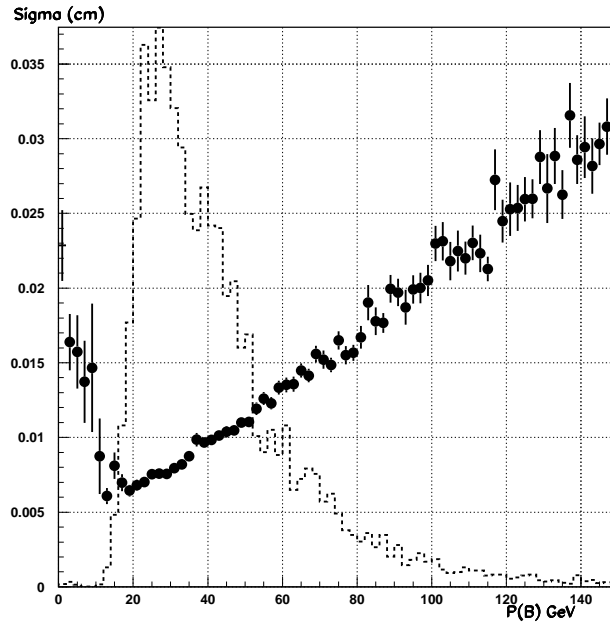


Figure 5: The  $B$  momentum distribution for  $B^0 \rightarrow \pi^+\pi^-$  events (dashed) and the error in decay length  $\sigma_L$  as a function of momentum.

Table 2: Level 1 trigger efficiencies for minimum-bias events and various processes of interest that are required to pass offline analysis cuts. All trigger efficiencies are determined for beam crossings with an average of two interactions per crossing using the Monte Carlo code shown in the table.

Process	Eff. (%)	Monte Carlo
Minimum bias	1	BTeVGeant
$B_s \rightarrow D_s^+ K^-$	74	BTeVGeant
$B^0 \rightarrow D^{*+} \rho^-$	64	BTeVGeant
$B^0 \rightarrow \rho^0 \pi^0$	56	BTeVGeant
$B^0 \rightarrow J/\psi K_s$	50	BTeVGeant
$B_s \rightarrow J/\psi K^{*o}$	68	MCFast
$B^- \rightarrow D^0 K^-$	70	MCFast
$B^- \rightarrow K_s \pi^-$	27	MCFast
$B^0 \rightarrow 2\text{-body modes}$ ( $\pi^+ \pi^-$ , $K^+ \pi^-$ , $K^+ K^-$ )	63	MCFast

detector, reconstructs the primary vertices and determines whether there are detached tracks which could signify a  $B$  decay. Since the  $b$ 's are at high momentum, the multiple scattering of the decay products is minimized allowing for triggering on detached heavy quark decay vertices.

With our outstanding pixel resolution, we are able to trigger efficiently at Level 1 on a variety of  $b$  decays. The trigger has been fully simulated, including the pattern recognition code. In Table 2 we give the efficiencies to trigger on a sample of final states providing that the particles are in the detector acceptance and otherwise pass all the analysis cuts. We see the trigger efficiencies are generally above 50% for the  $b$  decay states of interest and at the 1% level for minimum bias background. These numbers are evaluated at an average rate of 2 interactions per beam crossing, corresponding to our design luminosity of  $2 \times 10^{32} \text{ cm}^{-2} \text{ s}^{-1}$ .

#### 4.4 Charged Particle Identification

Charged particle identification is an absolute requirement for a modern experiment designed to study the decays of  $b$  and  $c$  quarks. The relatively open forward geometry has sufficient space to install a Ring Imaging Cherenkov detector (RICH), which provides powerful particle ID capabilities over a broad range of momentum. The BTeV RICH detector must separate pions from kaons and protons in a momentum range from 3 – 70 GeV/ $c$ . The lower momentum limit is determined by soft kaons useful for flavor tagging, while the higher momentum limit is given by two-body  $B$  decays. Separation is accomplished using a gaseous freon radiator to generate Cherenkov light in the optical frequency range. The light is then focused from mirrors onto Hybrid Photo-Diode (HPD) tubes. To separate kaons from protons below 10 GeV/ $c$  an aerogel radiator will be used.

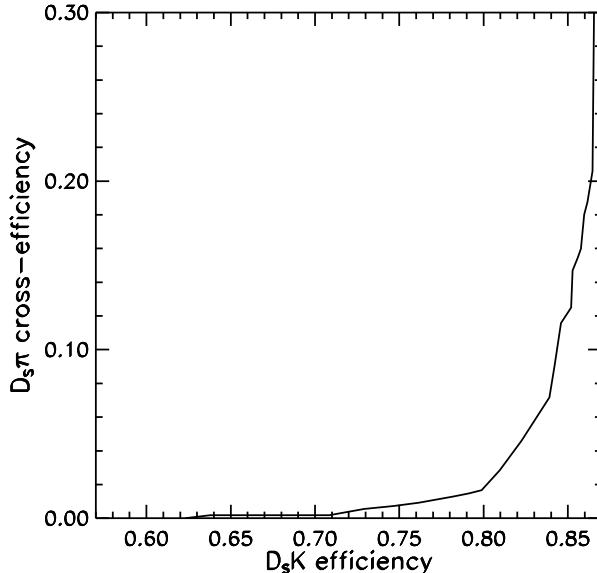


Figure 6: The efficiency to detect the fast  $K^-$  in the reaction  $B_s \rightarrow D_s^+ K^-$  versus the rate to misidentify the  $\pi^-$  from  $B_s \rightarrow D_s^+ \pi^-$  as a  $K^-$ .

As an example of the usefulness of this device we show, in Fig. 6, the efficiency for detecting the  $K^-$  in the decay  $B_s \rightarrow D_s^+ K^-$  versus the rejection for the  $\pi^-$  in the decay  $B_s \rightarrow D_s^+ \pi^-$ . We see that high efficiencies can be obtained with excellent rejections.

## 4.5 Electromagnetic Calorimeter

In BTeV, photons and electrons are detected when they create an electromagnetic shower cascade in crystals of  $\text{PbWO}_4$ , a dense and transparent medium that produces scintillation light. The amount of light is proportional to the incident energy. The light is sensed by photomultiplier tubes (or possibly hybrid photodiodes). The crystals are 22 cm long and have a small transverse cross-section, 26 mm  $\times$  26 mm, providing excellent segmentation. The energy and position resolutions are exquisite,

$$\frac{\sigma_E}{E} = \sqrt{\frac{(1.6\%)^2}{E} + (0.55\%)^2}, \quad (4)$$

$$\sigma_x = \sqrt{\frac{(3500 \mu\text{m})^2}{E} + (200 \mu\text{m})^2}, \quad (5)$$

where  $E$  is in units of GeV. This leads to an r.m.s.  $\pi^0$  mass resolution between 2 and 5  $\text{MeV}/c^2$  over the  $\pi^0$  momentum range 1 to 40  $\text{GeV}/c$ .

The crystals are designed to point at the center of the interaction region. They start at a radial distance of 10 cm with respect to the beam-line and extend out to 160 cm. They

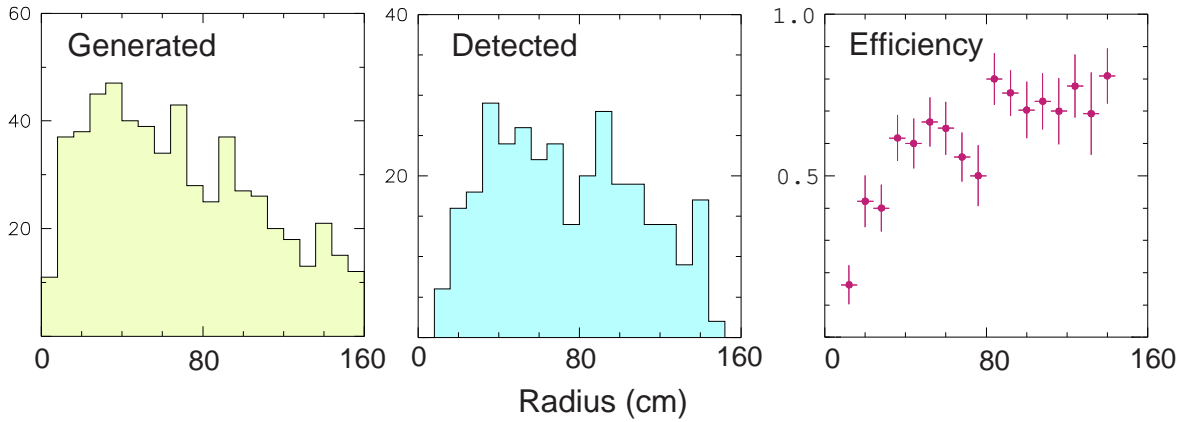


Figure 7: The radial distribution of generated and detected photons from  $B^0 \rightarrow K^*\gamma$  and the resulting efficiency. The detector was simulated by GEANT and the resulting crystal energies were clustered by our software. The charged tracks from the  $K^*$  were required to hit the RICH. The simulation was run at 2 interactions/crossing.

cover  $\sim 210$  mrad. This is smaller than the 300 mrad acceptance of the tracking detector; the choice was made to reduce costs. For most final states of interest this leads to a loss of approximately 20% in signal.

The calorimeter, at 2 interactions per crossing, has a high rate close to the beam pipe, where the reconstruction efficiency and resolution is degraded by overlaps with other tracks and photons. As we go out to larger radius, the acceptance becomes quite good. This can be seen by examining the efficiency of the  $\gamma$  in the decay  $B^0 \rightarrow K^*\gamma$ ,  $K^* \rightarrow K^-\pi^+$ . Here the decay products of the  $K^*$  are required to reach the RICH detector. Fig. 7 shows the radial distribution of the generated  $\gamma$ 's, the reconstructed  $\gamma$ 's and the  $\gamma$  efficiency versus radius. The shower reconstruction code, described in Chapter 12 of the proposal, was developed from that used for the CLEO CsI calorimeter; for reference, the efficiency of the CLEO barrel electromagnetic calorimeter is 89%.

## 4.6 Forward Tracking System

The other components of the charged-particle tracking system are straw-tube wire proportional chambers and, near the beam where occupancies are high, silicon microstrip detectors. These devices are used primarily for track momentum measurement,  $K_s$  detection and the Level 2 trigger. These detectors measure the deflection of charged particles by the BTeV analyzing magnet and give BTeV excellent mass and momentum resolution for charged particle decay modes.

## 4.7 Muon Detection

Muon detection is accomplished by insisting that the candidate charged track penetrate several interaction lengths of magnetized iron and insuring that the momentum determined from the bend in the toroid matches that given by the main spectrometer tracking system. The muon system is also used to trigger on the dimuon decays of the  $J/\psi$ . This is important not only to gather more signal but as a cross check on the efficiency of our main trigger, the Detached Vertex Trigger.

## 4.8 Data Acquisition System

BTeV has a data acquisition system (DAQ) which is capable of recording a very large number of events. The full rate of  $B$ 's whose decay products are in the detector is very high, over 1 kHz. The (direct) charm rate is similar. Other experiments are forced by the limitations of their data acquisition system to make very harsh decisions on which  $B$  events to take. BTeV can record nearly all the potentially interesting  $B$  and charm candidates in its acceptance. Therefore it can address many topics that might be discarded by an experiment whose DAQ is more restrictive. Since nature has a way of surprising us, we view the open nature of the BTeV trigger and the capability of the DAQ as a genuine strength that offers us the opportunity to learn something new and unanticipated.

# 5 Simulation Results and Physics Reach

The physics reach of BTeV has been established by an extensive and sophisticated program of simulations, which is described in detail in Part 3 of the proposal. We have simulated the efficiencies and backgrounds in the decay modes used to measure the CP violating angles  $\alpha$ ,  $\beta$ ,  $\gamma$  and  $\chi$ , the  $B_s$  mixing parameter  $x_s$  and a few rare decay final states.

We have used two simulation packages, GEANT and MCFast. These tools and their use are explained in the beginning of Part III. Briefly, GEANT models all physical interactions of particles with material and allows us to see the effects of hard to calculate backgrounds. The goal of MCFast is to provide a fast, parametrized simulation which is more flexible than GEANT but not quite as complete in its modeling of physics processes.

In Table 3 we give the decay mode, the number of signal events found in  $10^7$  seconds at a luminosity of  $2 \times 10^{32} \text{ cm}^{-2}\text{s}^{-1}$  and the signal/background ratio for many of the interesting decay modes which are possible for BTeV. We also estimate the error in the relevant physics parameter, if possible, or the reach in  $B_s$  mixing. In some cases more than one reaction is used to determine a value; in that case they are put between horizontal lines.

Fig. 8 shows the power of an  $L/\sigma_L$  cut on reducing prompt backgrounds in order to extract a clean  $B \rightarrow J/\psi K_s^0$  signal. This rejection power comes from the forward geometry combined with excellent vertex resolution. Fig. 9 shows the superb capabilities of the electromagnetic calorimeter in detecting photons that are used to reconstruct  $\eta$  and  $\eta'$  candidates, which can be combined with  $J/\psi$ 's to measure  $\chi$  through the state  $B_s \rightarrow J/\psi \eta^{(\prime)}$ . Fig. 10 shows the

Table 3: Summary of physics reach in  $10^7$ s. Pairs of reactions between two lines are used together.

Process	# of Events	$S/B$	Parameter	Error or (Value)
$B^o \rightarrow \pi^+\pi^-$	24,000	3	Asym.	0.024
$B_s \rightarrow D_s^\pm K^\mp$	13,100	7	$\gamma$	$7^\circ$
$B^o \rightarrow J/\psi K_S$	80,500	10	$\sin(2\beta)$	0.025
$B_s \rightarrow D_s^+ \pi^-$	103,000	3	$x_s$	(75)
$B^- \rightarrow \overline{D^0}(K^+\pi^-)K^-$	300	1	$\gamma$	$10^\circ$
$B^- \rightarrow D^0(K^+K^-)K^-$	1,800	$>10$	$\gamma$	$10^\circ$
$B^- \rightarrow K_S \pi^-$	8,000	1	$\gamma$	$< 5^\circ$
$B^o \rightarrow K^+ \pi^-$	108,000	20	$\gamma$	$< 5^\circ$
$B^o \rightarrow \rho^\pm \pi^\mp$	9,400	4.1	$\alpha$	$\sim 10^\circ$
$B^o \rightarrow \rho^o \pi^o$	1,350	0.3	$\alpha$	$\sim 10^\circ$
$B_s \rightarrow J/\psi \eta$	1,920	15	$\sin(2\chi)$	0.033
$B_s \rightarrow J/\psi \eta'$	7,280	30	$\sin(2\chi)$	0.033
$B^- \rightarrow K^- \mu^+ \mu^-$	1280	3.2		
$B^o \rightarrow K^* \mu^+ \mu^-$	2200	10		

decay mode  $B_s \rightarrow D_s K$  signal which can be used to measure  $\gamma$ . The  $\pi^+\pi^-\pi^o$  invariant mass distributions for  $B \rightarrow \rho\pi$  signal and background are shown in Fig. 11. The  $B \rightarrow \rho\pi$  decay can be used to measure  $\alpha$ .

The physics reach of BTeV is extraordinary, even in just one year of running. BTeV will be the first to make a precision measurement of the angle  $\gamma$ ; this will be accomplished in one year of running. The angles  $\alpha$  and  $\chi$  will also be measured, though this will take a bit longer. The  $B_s$  mixing reach is up to  $x_s$  of 75, well above the Standard Model allowed range of about 40. Thus, not only can BTeV measure the value in the Standard Model, but it also has a good chance to measure  $B_s$  mixing if it is determined by physics beyond the Standard Model. Non-Standard Model physics can also be seen via rare decays where large numbers of reconstructed events are expected.

## 6 Comparisons With Other Experiments

BTeV compares favorably to all other heavy quark experiments.

BTeV has considerably more reach in every physics channel than  $e^+e^-$   $B$  factories. We give one example here. Table 4 shows a comparison between BTeV and an asymmetric  $e^+e^-$  machine for measuring the CP violating asymmetry in the decay mode  $B^o \rightarrow \pi^+\pi^-$ . It is clear that the large hadronic  $b$  production cross section can overwhelm the much smaller  $e^+e^-$  rate. Furthermore, the  $e^+e^-$   $B$  factories do not have access to the important CP violation measurements that need to be made in  $B_s$  decays. Nor can they explore potentially interesting topics in the physics of  $b$ -baryons and  $B_c$  mesons.

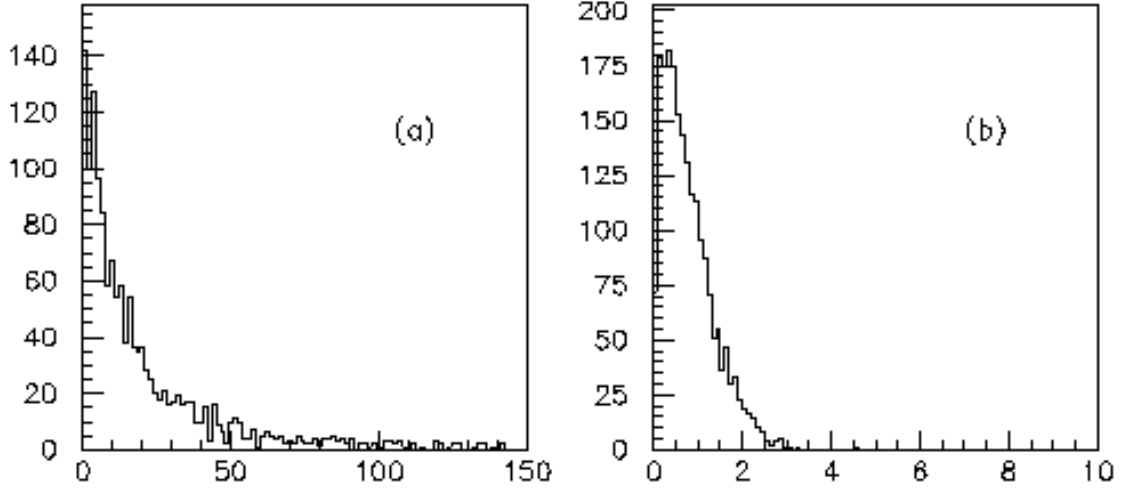


Figure 8: Distributions of  $L/\sigma_L$  for (a)  $J/\psi$  candidates from  $B^0 \rightarrow J/\psi K_s$  and (b) prompt  $J/\psi$  candidates. The prompt candidates are suppressed by requiring  $L/\sigma_L > 4$ .

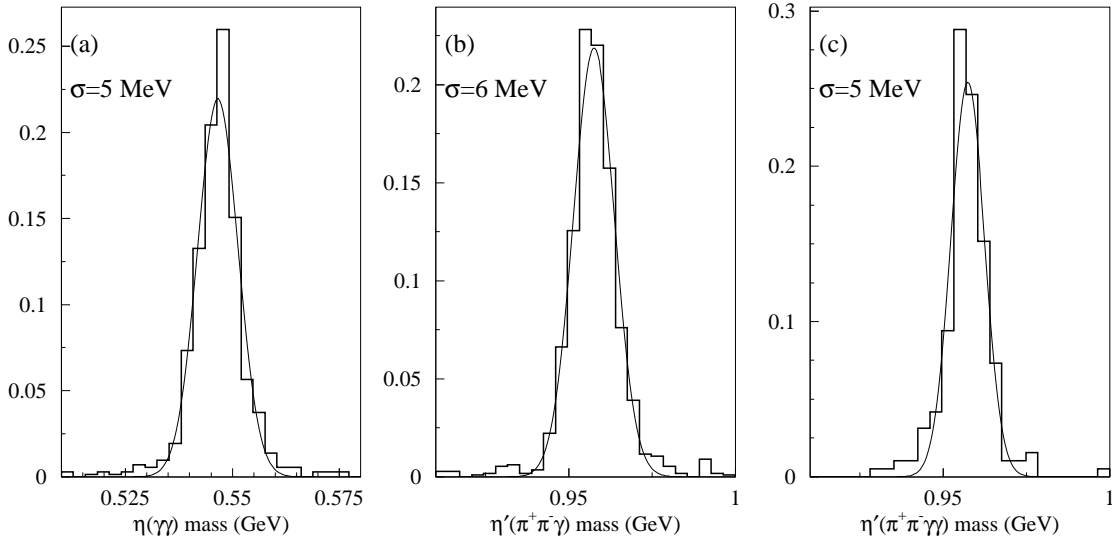


Figure 9: The invariant mass distributions for (a)  $\eta \rightarrow \gamma\gamma$ , (b)  $\eta' \rightarrow \pi^+\pi^-\gamma$ , and  $\eta' \rightarrow \pi^+\pi^-\eta$ ,  $\eta \rightarrow \gamma\gamma$ . The Gaussian mass resolutions are indicated.  $\eta$  and  $\eta'$  candidates can be used to measure  $\chi$  using the decay mode  $B_s \rightarrow J/\psi\eta'$  and  $B_s \rightarrow J/\psi\eta$ .

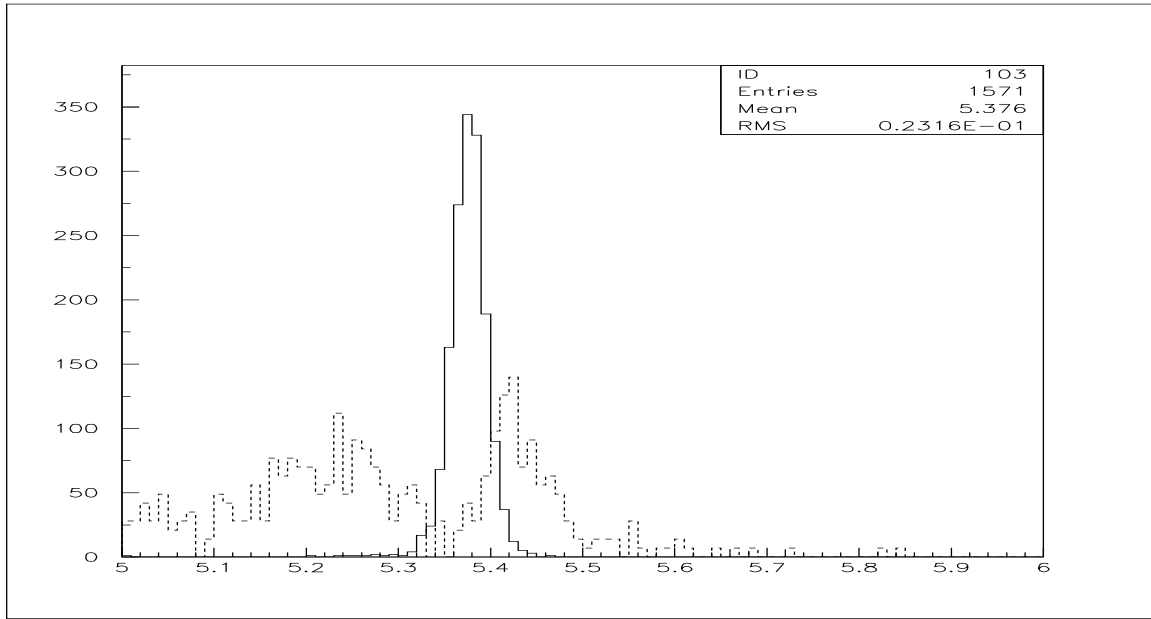


Figure 10: Comparison of  $B_s \rightarrow D_s^+ K^-$  signal and background from  $B_s \rightarrow D_s X$ , where X contains at least one pion misidentified as a  $K^-$ . This state is used to measure  $\gamma$ .

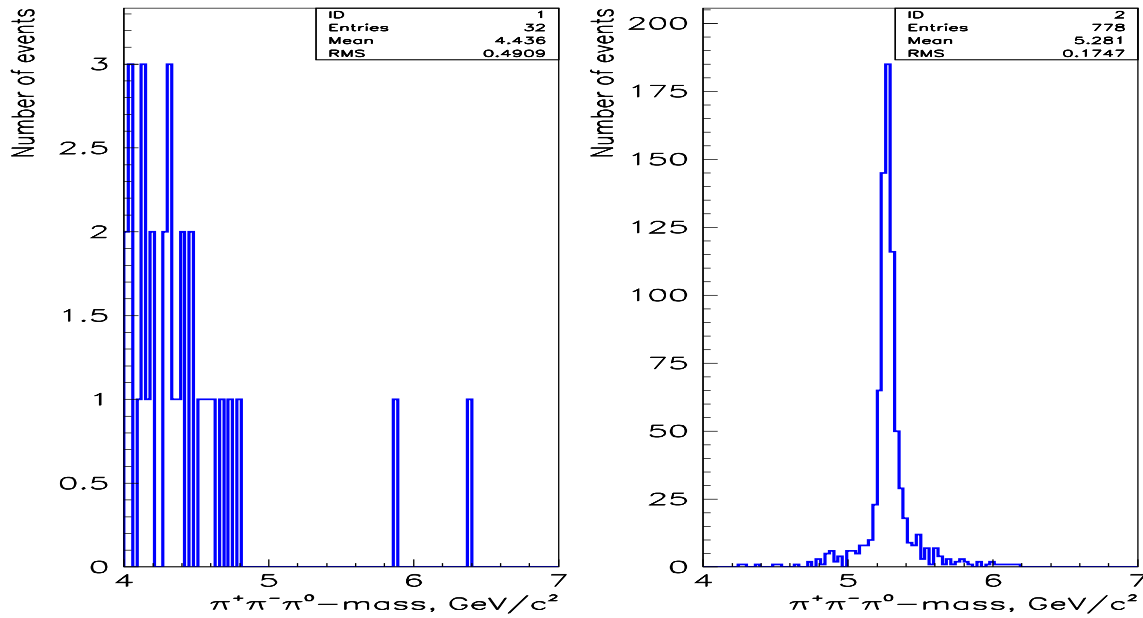


Figure 11: Invariant  $\pi^+ \pi^- \pi^0$  mass distributions for background (left) and signal (right) events for  $B \rightarrow \rho^+ \pi^-$ . This state is used to measure  $\alpha$ . (The background is not normalized to the signal).



Table 4: Number of tagged  $B^o \rightarrow \pi^+\pi^-$  ( $\mathcal{B}=0.43 \times 10^{-5}$ ).

	$\mathcal{L}(\text{cm}^{-2}\text{s}^{-1})$	$\sigma$	# $B^o/10^7$ s	Signal	Tagging	# Tagged/ $10^7$ s
				Efficiency	$\epsilon D^2$	
$e^+e^-$	$3 \times 10^{33}$	1.2 nb	$3.6 \times 10^7$	0.3	0.3	13
BTeV	$2 \times 10^{32}$	100 $\mu$ b	$1.5 \times 10^{11}$	0.037	0.1	2370

CDF and D0 have done useful  $b$  physics by triggering on  $J/\psi$  decays into dimuons. CDF plans more aggressive triggers on selected purely hadronic final states in the future. However, the kinematics of  $b$  decays do not favor the central region. Most of the  $b$ 's are relatively slow with the peak of the transverse momentum distribution being at 5.3 GeV/ $c$ , which at an  $\eta$  of 1, produces  $B$ 's with  $\gamma\beta$  of 1. These relatively slow  $B$ 's are intrinsically difficult to vertex and trigger on. Furthermore, CDF and D0 do not have state of the art charged particle identification nor do they possess excellent photon detection.

Although the ATLAS and CMS detectors will have some  $b$  physics capabilities, they will be limited to final states with dileptons or even perhaps only to  $J/\psi$  decays. LHC-b, on the other hand, is an experiment that has been designed exclusively to study  $b$  decays and provides real competition in many areas. Our simulations show that we expect larger yields than LHC-b in all charged particle final states, at comparable or better signal-to-noise ratios, and we have large advantages in final states with photons.

For example, we compare the reaction  $B^o \rightarrow \rho\pi$  in Table 5. Both sets of numbers are calculated for  $10^7$  seconds at a luminosity of  $2 \times 10^{32} \text{ cm}^{-2}\text{s}^{-1}$ . We have corrected the LHC-b numbers by normalizing them to the branching ratios used by BTeV.

Table 5: Event yields and signal/background for  $B^o \rightarrow \rho\pi$ .

Mode	Branching Ratio	BTeV		LHC-b	
		Yield	S/B	Yield	S/B
$B^o \rightarrow \rho^\pm\pi^\mp$	$2.8 \times 10^{-5}$	9400	4.1	2140	0.8
$B^o \rightarrow \rho^o\pi^0$	$0.5 \times 10^{-5}$	1350	0.3	880	-

Furthermore, we intend to output on the order of 5 times more  $b$ 's per second than LHC-b allowing for a greater range of physics studies. We also have the capacity in our data acquisition system to accept a large number of directly produced charm decays.

## 7 Conclusion

BTeV is a powerful and precise scientific instrument capable of exquisite tests of the Standard Model. It has great potential to discover new physics via rare or CP violating decays of heavy

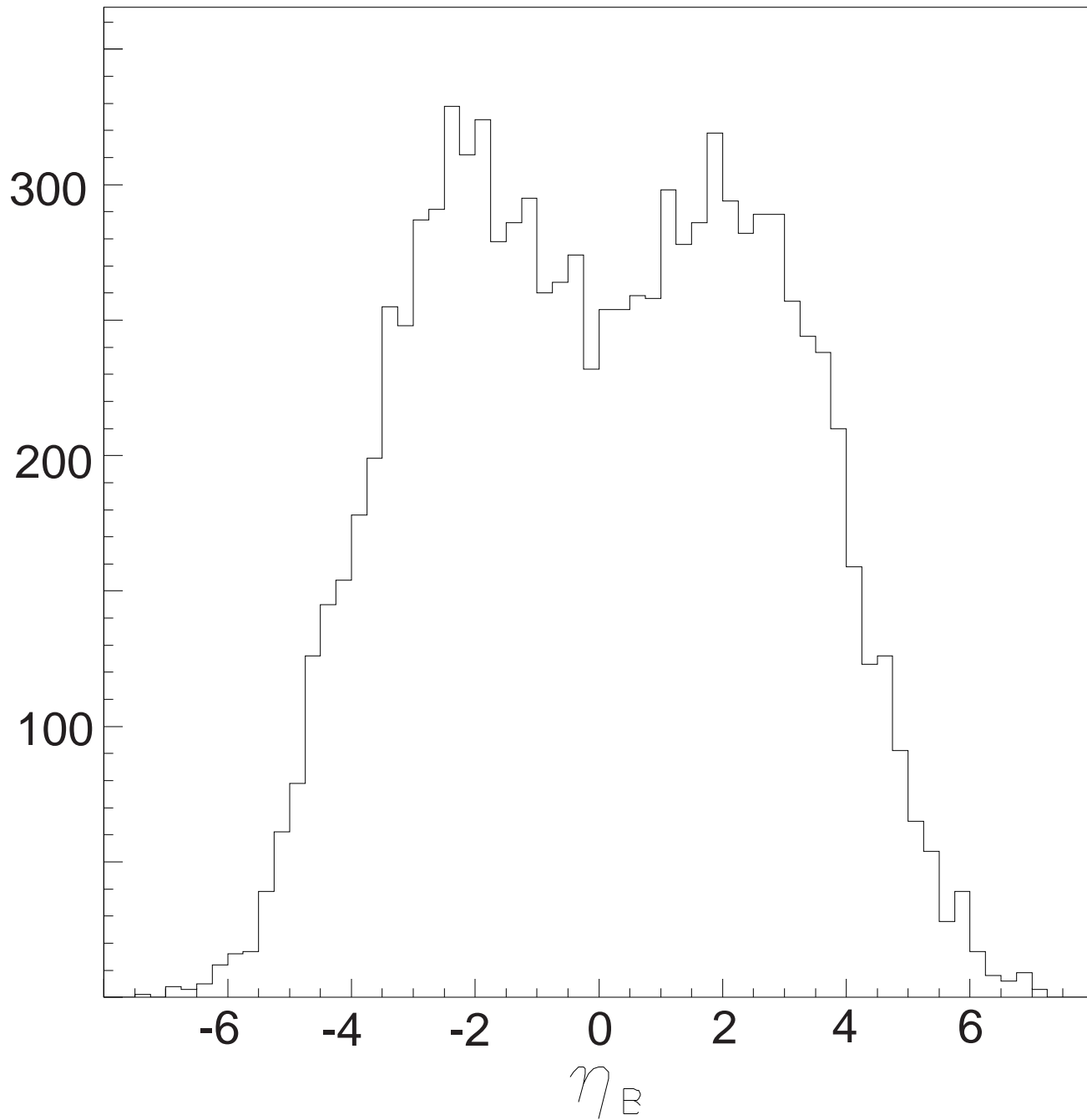
quarks.

## Acknowledgements

This work received partial support from Fermilab which is operated by University Research Association Inc. under Contract No. DE-AC02-76CH03000 with the United States Department of Energy.

## References

- [1] N. Cabibbo, *Phys. Rev. Lett.* **10**, 531 (1963); M. Kobayashi and K. Maskawa, *Prog. Theor. Phys.* **49**, 652 (1973).
- [2] R. Aleksan, B. Kayser and D. London, *Phys. Rev. Lett.* **73** (1994) 18 (hep-ph/9403341).
- [3] F. Abe *et al.*, “Measurement of the  $B$  Meson Differential Cross-Section in  $p\bar{p}$  collisions at  $\sqrt{s} = 1.8$  TeV,” CDF/PUB/BOTTOM/PUBLIC/3759 submitted to ICHEP '96 and references therein; F. Abe *et al.*, *Phys. Rev. Lett.* **75**, 1451 (1995); R. Abbott *et al.*, “The  $b\bar{b}$  Production Cross Section and Angular Correlations in  $p\bar{p}$  collisions at  $\sqrt{s} = 1.8$  TeV,” FERMILAB-Pub-99/144-E; S. Abachi *et al.*, *Phys. Rev. Lett.* **74**, 3548 (1995).
- [4] D. Fein, “Tevatron Results on  $b$ -Quark Cross Sections and Correlations,” presented at Hadron Collider Physics (HCP99) (Bombay), January 1999.



# List of Figures

1.1	The six CKM triangles. The bold labels, i.e <b>ds</b> refer to the rows or columns used in the unitarity relationship. . . . .	5
1.2	The CKM triangle shown in the $\rho - \eta$ plane. The left side is determined by $ V_{ub}/V_{cb} $ and the right side can be determined using mixing in the neutral $B$ system. The angles can be found by making measurements of CP violation in $B$ decays. . . . .	6
1.3	The two diagrams for $B_d$ mixing. . . . .	6
1.4	The regions in $\rho - \eta$ space (shaded) consistent with measurements of CP violation in $K_L^0$ decay ( $\epsilon$ ), $V_{ub}/V_{cb}$ in semileptonic $B$ decay, $B_d^0$ mixing, and the excluded region from limits on $B_s^0$ mixing. The allowed region is defined by the overlap of the 3 permitted areas, and is where the apex of the CKM triangle sits. . . . .	8
1.5	Diagrams for $B^- \rightarrow K^- \pi^0$ , (a) and (b) are tree level diagrams where (b) is color suppressed; (c) is a penguin diagram. (d) shows $B^- \rightarrow K^0 \pi^-$ , which cannot be produced via a tree diagram. . . . .	9
1.6	Two interfering ways for a $B^0$ to decay into a final state $f$ . . . . .	11
1.7	Decay diagram at the tree level for $B^0 \rightarrow \pi^+ \pi^-$ . . . . .	13
1.8	Decay diagram at the tree level for $B^0 \rightarrow J/\psi K_S$ . . . . .	13
1.9	The decay rates for $B^0 \rightarrow J/\psi K^0$ , $K^0 \rightarrow \pi \ell \nu$ , as a function of $K^0$ decay time, integrated over the $B^0$ decay time. The solid lines have the sign of the $\cos(2\beta)$ term as positive, while the corresponding dashed lines have negative values. The absolute normalization is arbitrary, and $\sin(2\beta)$ was fixed at 0.7. . . . .	16
1.10	Penguin diagram for $B^0 \rightarrow \pi^+ \pi^-$ . . . . .	17
1.11	The Dalitz plot for $B^0 \rightarrow \rho \pi \rightarrow \pi^+ \pi^- \pi^0$ from Snyder and Quinn. . . . .	19
1.12	Two diagrams for $\overline{B}_s^0 \rightarrow D_s^\pm K^\mp$ . . . . .	20
1.13	Diagrams for the two interfering processes, (a) $B^- \rightarrow D^0 K^-$ (color allowed) followed by $D^0 \rightarrow K^+ \pi^-$ (doubly-Cabibbo suppressed), and (b) $B^- \rightarrow \overline{D}^0 K^-$ (color suppressed) followed by $D^0 \rightarrow K^- \pi^+$ (Cabibbo allowed). . . . .	21
1.14	Contour plots from Neubert [55] for the quantities $R_*$ (“hyperbolas”) and $\tilde{A}$ (“circles”) plotted in the $\phi - \gamma$ plane. The units are degrees. The scatter plots show the results including rescattering effects, while the lines refer to $\epsilon_a = 0$ . The solid curves correspond to the contours for $R_* = 0.7$ and $\tilde{A} = 0.2$ , the dashed ones to $R_* = 0.9$ and $\tilde{A} = 0.4$ . . . . .	24

1.15	Feynman diagrams contributing to $B_d \rightarrow \pi^+\pi^-$ and $B_s \rightarrow K^+K^-$ (from Fleischer).	25
1.16	The “allowed” values for the three angles of the CKM triangle derived from the allowed, i.e. $1\sigma$ overlap, region of Fig. 1.4.	31
1.17	Loop or “Penguin” diagram for a $b \rightarrow s$ or $b \rightarrow d$ transition.	33
1.18	The background subtracted photon energy spectrum from CLEO. The dashed curve is a spectator model prediction from Ali and Greub.	34
1.19	Loop or “Penguin” diagram for a $b \rightarrow s\ell^+\ell^-$ transition.	35
1.20	Decay diagrams resulting in dilepton final states. (a) is an annihilation diagram, and (b) is a box diagram.	36
2.1	Layout of BTeV/C0 Spectrometer	46
2.2	The $b\bar{b}$ cross-section as a function of the rapidity of muons from $b$ decay, $y^\mu$ , measured by D0 for both the forward and central rapidity regions, using muons from $b$ decays with $p_t > 5$ GeV/c. The solid curve is the prediction of the next-to-leading order QCD calculation for a $b$ -quark mass of 4.75 GeV. The dashed curves represent the estimated theoretical $1\sigma$ error band.	47
2.3	The $B$ yield versus $\eta$ .	48
2.4	$\beta\gamma$ of the $B$ versus $\eta$ .	49
2.5	The differential $\delta\phi$ cross-sections for $p_T^\mu > 9$ GeV/c, $ \eta^\mu  < 0.6$ , $E_T^{\bar{b}} > 10$ GeV, $ \eta^{\bar{b}}  < 1.5$ compared with theoretical predictions. The data points have a common systematic uncertainty of $\pm 9.5\%$ . The uncertainty in the theory curve arises from the error on the muonic branching ratio and the uncertainty in the fragmentation model.	49
2.6	The production angle (in degrees) for the hadron containing a $b$ quark plotted versus the production angle for a hadron containing $\bar{b}$ quark, from the Pythia Monte Carlo generator.	50
3.1	C0 Collision Hall	53
3.2	Tevatron berm and C0 Assembly Building	54
3.3	Layout of C0 Collision Area	55
3.4	Cross section of the modified SM3 dipole with rollers and pole piece inserts. All dimensions are in inches.	57
3.5	Fraction of events with N primary tracks above 1 GeV/c momentum for a) a dipole centered on the IR giving an effective two-arm acceptance and b) a single forward spectrometer arm.	58
3.6	Schematic of Muon toroid.	59
3.7	Schematic of the tracking detectors and beampipe.	60
4.1	Schematic drawing of part of the pixel detector.	62
4.2	Pixels on the half plane.	65
4.3	Sample fuzzy carbon composites; note the shingling in the picture on the right.	66
4.4	Side view of the vacuum vessel and support structure for the pixel detector.	66

4.5	Multiparticle interaction observed in Fermilab beam test. This density of tracks is much higher than expected in the BTeV pixel detector. . . . .	68
4.6	Resolution as a function of the angle of the incident beam. . . . .	69
5.1	Occupancies in the first station of straws, and the station just upstream of the RICH counter, when a $b\bar{b}$ event is produced at the design luminosity of $2 \times 10^{32} \text{ cm}^{-2} \text{ s}^{-1}$ . The two histograms on the left are for X-view straws, while those on the right are for U-view straws. The V-views have identical occupancies (mirrored about zero) to the U-views. . . . .	74
5.2	Sketch of a silicon detector plane. It consists of 4 ladders of two daisy-chained Si-sensors plus 2 single sensors. One strip overlap between contiguous detector elements ensures good efficiency over the entire plane. Dimensions are in centimeters and <i>F.E.</i> stands for Front-End read out electronics. . . . .	76
5.3	Radiation dose as a function of position in Forward Silicon Tracker Station # 1. The horizontal magnetic field concentrates more particles above and below the square central beam hole than on either side. . . . .	78
5.4	Momentum resolution as a function of track momentum for $b$ decay products. . . . .	79
5.5	Momentum resolution as a function of polar production angle for $b$ decay products. . . . .	79
6.1	The momentum distribution of pions in $B_d \rightarrow \pi^+\pi^-$ decays. The left plot shows distributions for the lower (dashed line) and higher (solid line) momentum pion in this decay. The right plot presents the latter distribution in integral form, which gives loss of efficiency as a function of the high momentum cut-off of the particle ID device. . . . .	82
6.2	The momentum distribution of “tagging” kaons for the case where the signal particles ( $\psi K_S^0$ ) are within the geometric acceptance of the spectrometer. The left plot shows distributions for kaons absorbed in (dashed line) and exiting from (solid line) the magnet. The right plot presents the latter distribution in integral form, which gives loss of efficiency as a function of the low momentum cut-off of the particle ID device. . . . .	83
6.3	Cherenkov angles for various particle species as a function of particle momentum for $C_4F_{10}$ and aerogel ( $n = 1.03$ ) radiators. . . . .	84
6.4	BTeV RICH geometry outline. . . . .	85
6.5	PP0380V HPD from DEP (on the left) and possible pixel structure on HPD silicon diode (on the right). Only parts inside the circular area would be actually implemented. Dimensions are expressed in mm. . . . .	87
6.6	Efficiency for $B_d \rightarrow \pi^+\pi^-$ as a function of the cost of the photo-detectors. Efficiency is defined relative to the reconstructed events with both tracks crossing the RICH detector. Each track was required to have enough photons for $4\sigma$ K/ $\pi$ separation (from the gaseous radiator alone). Effects due to Cherenkov ring overlaps are not taken into account. The actual choice of a size of the HPD system is shown by vertical line. . . . .	89

6.7	A typical reconstructed $B_d \rightarrow \pi^+\pi^-$ event. Gaseous and aerogel Cherenkov photons radiated by the signal pions are highlighted. . . . .	90
6.8	Cross-efficiency of particle identification system for $B_d \rightarrow K^\pm\pi^\mp$ and $B_s \rightarrow K^+K^-$ as a function $B_d \rightarrow \pi^+\pi^-$ particle identification efficiency. The efficiencies are defined relative to the number of events with both tracks entering the RICH detector. The Monte Carlo simulation included an average of two minimum bias interactions in addition to the $b\bar{b}$ production. . . . .	91
7.1	The efficiency as a function of calorimeter radius for the reaction $\bar{B}^0 \rightarrow D^{*+}\rho^-$ .	96
7.2	The energies in the PbWO <sub>4</sub> calorimeter (one end) for an event containing two photons from the decay sequence $B^0 \rightarrow \rho^0\pi^0$ , $\pi^0 \rightarrow \gamma\gamma$ . The photons of energies 19.3 and 2.4 GeV are surrounded by large circles. All energies above 10 MeV are shown, with the height of line proportional to the energy. . . . .	97
7.3	(left) The maximum dose distribution in the crystals for for 1 year of running at a luminosity of $2 \times 10^{32}\text{cm}^{-2}\text{s}^{-1}$ . (right) The integral of the maximum dose distribution. . . . .	98
7.4	The $\gamma\gamma$ invariant mass for 10 GeV $\pi^0$ 's incident on the calorimeter. The fit is to a Gaussian signal function plus a polynomial background. . . . .	99
7.5	The difference between the measured and generated energies, divided by the generated energy, for reconstructed photons as simulated by GEANT for BTeV (left) and CLEO (right). The photons candidate clusters were required to have shower energy shapes consistent with that expected for photons and to be isolated from charged tracks. The BTeV simulation was run at 2 interactions/crossing. . . . .	100
7.6	The radial distribution of generated and detected photons from $B^0 \rightarrow K^*\gamma$ and the resulting efficiency. The detector was simulated by GEANT and the resulting crystal energies were clustered by our software. The charged tracks from the $K^*$ were required to hit the RICH. The simulation was run at 2 interactions/crossing. . . . .	101
7.7	The efficiency as a function of the radial distance from the beam line of $\pi^0$ 's from $B \rightarrow \rho\pi$ decays at the position of the calorimeter. The simulation was run at 2 interactions/crossing in the "large" calorimeter. . . . .	101
8.1	(left) Efficiency, calculated in a simple Gaussian model, for a muon with 1/10 the threshold momentum to pass a momentum threshold as a function of $a$ , the MCS term in the resolution formula. (right) Efficiency as a function of muon momentum for a trigger designed to fire with a 50% efficiency at 10 GeV. The multiple scattering dominated term is fixed ( $a = 25\%$ ) while the measurement dominated term varies from $1\%/\text{GeV} < b < 10\%/\text{GeV}$ . . . . .	104

8.2	Layout of the baseline geometry, shown in elevation view. The three dark boxes, labelled $\mu_1, \mu_2$ , and $\mu_3$ , represent detector stations with 4 measurement views per station. The two lighter boxes with lengths of 1 m represent magnetized steel toroids, which provide bending power for the muon momentum measurement and which also serve as hadron absorbers. The 30 cm long lighter box is an unmagnetized iron shield. The downstream trajectory is measured by $\mu_2$ and $\mu_3$ . The upstream trajectory is measured using the nominal beam center with possible help from $\mu_1$ . To obtain sufficient bending power, both 1 m steel sections must be magnetized. . . . .	105
8.3	End and top views of one “plank” of proportional tubes. . . . .	106
8.4	Plots of the fractional momentum resolution versus momentum for various muon system configurations. All plots assume 2.5 mm RMS spatial resolution. The plots appear in groups of 3 corresponding to $\phi = 270^\circ$ (best) $0^\circ$ and $90^\circ$ (worst). The $\phi$ dependence illustrates interference between the central dipole and muon toroid(s). The top (bottom) curves show the resolution when one (two) toroids are magnetized. The black and red curves illustrate the case where only the two stations after the second toroid are used. In this case the trajectory upstream of the toroid comes entirely from the beam constraint. The blue and magenta curves illustrate the case where the station between the two toroids is used to help determine the trajectory prior to the toroids. The green curves assume only the final two stations are used, and the dipole is turned off. . . . .	107
8.5	(left) Beams-eye view of one muon detector station, which consists of eight overlapping octants arranged in two layers. One octant is cut away in places to show the overlap between adjacent octants. (right) Arrangement of planks to form the four views in an octant ( $r$ view is repeated). There will be 13 planks per view (more than shown). . . . .	107
8.6	Characteristics of muon detector hits for $J/\psi K_s^0$ events. (a) Particle type. Each particle type is assigned an integer code, shown in the legend. For example, $\pi^+$ is given the code 8. The electromagnetic and hadronic noise is larger than the muon signal. The excess of electrons over positrons is due to $\delta$ -ray production. (b) Projected radial position at the downstream face of the second filter for tracks that hit station 3. The large percentage of tracks emanating from the vicinity of the hole in the filter is quite evident. (c) and (d) Momentum of pion and $e^+/e^-$ noise. Noise secondaries have much lower momentum than $J/\psi$ muons. . . . .	110
8.7	Distribution of hits among muon detector planes for different shielding configurations. There are twelve planes per station. (a: upper left) Original design; no extra shielding. (b: lower left) Extra shielding block in front of the third station. (c: Upper right) Extra shielding around the beam pipe. (d: Lower right) Both beam pipe and third station shielded. . . . .	111



8.8	<i>J/ψ</i> efficiency versus minimum bias rejection rate for cuts on the minimum radius, maximum $\chi^2$ , and the minimum muon $P_T$ . Two oppositely charged tracks in different octants in the same arm must pass the relevant cut. Black lines connect the squares which show the variation as the minimum radius is increased. From each black square a red line connecting the circles shows the change as the maximum $\chi^2$ cut is decreased. From each red circle a green line connecting the triangles shows the variation as the minimum reconstructed muon $P_T$ is increased. All information in this stand-alone trigger comes from hits in the muon system alone. . . . .	112
8.9	<i>J/ψ</i> efficiency versus minimum bias rejection rate, using a simplified tracking trigger, for cuts on the minimum radius, minimum muon $p_T$ , and the minimum muon momentum. Two oppositely charged tracks in different octants in the same arm must pass the relevant cut. Black lines connect the squares which show the variation as the minimum radius is increased.. From each black square a red line connecting the circles shows the change as the minimum muon $p_T$ cut is increased. From each red circle a green line connecting the triangles shows the variation as the minimum muon momentum is increased. . . . .	113
9.1	Overview of the three-level trigger system. . . . .	118
9.2	Block diagram of proposed DAQ system indicating design bandwidths before and after the Level 1 trigger: up to 1500 GBytes/s of data are digitized from detector subsystems and stored in Level 1 buffers, and up to 25 GBytes/s are passed to Levels 2 and 3. . . . .	121
9.3	Block diagram of the baseline Level 1 trigger. . . . .	122
9.4	Sketch of pixel planes showing (shaded) “inner” and “outer” frames within which track seeds are sought. In the figure, track seeds for the track near the top of the figure are found in the first and last tracking stations. For the lower track the seeds are found in the second and second-to-last stations. . . . .	123
9.5	Segment-finding “kernel” consisting of an associative memory (AM) with cut and projection operators. . . . .	124
9.6	Use of a “virtual hit” in finding track segments. The open point with error bars is the virtual hit, while the full points are pixel clusters in planes $N$ and $N - 1$ . . . . .	125
9.7	Schematic of a “unit cell” of the segment-finding hardware. . . . .	126
9.8	Track reconstruction efficiency <i>vs.</i> momentum for tracks that are contained within the fiducial volume of the vertex detector. Tracks are required to enter the detector from the beam region, traverse at least four tracking stations, and exit the pixel detector. Data points with squares show the tracking efficiency, which is about 95% above 5 GeV/ $c$ , prior to clean-up cuts. Data points with asterisks show the efficiency after clean-up cuts. . . . .	128

9.9	a) trigger efficiencies for $B^o \rightarrow D^{*+} \rho^-$ , $D^{*+} \rightarrow \pi^+ D^o$ , $D^o \rightarrow K^- \pi^+$ for various detachment requirements for an average of two interactions/crossing, and b) the trigger response for minimum-bias crossings with the same detachment requirements. Trigger efficiencies are plotted <i>vs.</i> normalized impact parameter $m$ for $n = 1, 2, 3$ , and 4 detached tracks. The arrows indicate the Level 1 cut requiring $n = 2$ and $m > 6$ , which gives a minimum-bias rejection of 99%.	129
12.1	The BTeV spectrometer as drawn by BTeVGeant in elevation view (upper figure) and plan view (lower figure). The total length of this representation of the C0 Hall is about 26 m. . . . .	159
12.2	The Pixel detector and the hemispherical window, elevation view. The pixel region is 128 cm long. The 31 stations are clearly visible, except the central one which is masked by a structural support. The lines surrounding the planes within a station are fiducial, or buffer volumes, to ease the tracking debugging and do not correspond to real material. The medium inside the tank is vacuum. . . . .	160
12.3	The Pixel detector, beam's eye view, showing the layout of the pixel wafers (center), the cooling tube manifolds (left and right, thick lines), the main cooling tube (circle in each corner), the support structure (section of the arc, top and bottom) and the vacuum tank walls. The vacuum tank is 20 inches in diameter. In order to provide the beam hole, the center cell of the $9 \times 9$ array of pixel wafers is not present. . . . .	161
12.4	An elevation view of the region centered around $z=+1.6$ m, showing straw tube stations 2 and 3; each station consists of three views and three planes per view for a total of 9 planes per station. Upstream and downstream of each straw tube station are forward silicon strip planes and their support structure.	162
12.5	A beam's eye view of the muon detector, showing the beampipe shielding, the hadron filter and the layout of the muon planks. . . . .	163
12.6	An elevation view of the region from 7.8 m to 11.4 m, showing muon stations 1, 2 and 3. Also shown are the hadron filters and the beam pipe shielding. . . . .	164
12.7	Histograms of $m_{\gamma\gamma}$ for the four different sets of cuts: (upper left) $cutele = 500$ keV, $cutgam = 65$ keV; (upper right) $cutele = 1$ MeV, $cutgam = 65$ keV; (lower left) $cutele = 1$ MeV, $cutgam = 1$ MeV; (lower right) $cutele = 1$ MeV, $cutgam = 3$ MeV. . . . .	166
12.8	The $\pi^0$ mass resolution ( $\sigma =$ width of the mass peak) and the ratio of $\pi^0$ 's/background for the four different sets of gamma and electron cutoffs. The horizontal axis refers to the 4 sets of cuts shown in Figure 12.7. . . . .	167
12.9	The energy resolution ( $\frac{\sigma(E)}{E}$ ) and the width of the showers for different gamma and electron cutoff values . . . . .	167
12.10	The BTeVGeant simulation time for $D^* \rho$ events for the four different sets of cuts. The horizontal axis refers to the 4 sets of cuts shown in Figure 12.7. . . . .	168

12.11	The distributions of a) $\tan \theta_x$ and b) $\tan \theta_y$ for hits on tracks, in $b\bar{b}$ events, with at least 20 hits. Here $\theta_x$ is the angle of incidence, in the $xz$ plane, of a track which intersects a pixel detector. Similarly for $\theta_y$ . For most studies reported in this document, the pixel detectors are modeled as having a spatial resolution function which is Gaussian. The dependence of the $\sigma$ of the Gaussian on angle of incidence is shown in c) for pixels which measure $x$ and in d) for pixels which measure $y$ . In both cases the solid line shows the value of $\sigma$ for the short dimension while the dashed line shows the value for the pitch divided by $\sqrt{12}$ . . . . .	176
12.12	KNO scaling in MCFast: The scaled number of secondaries, $n_{sec}/n_{ave}$ , as generated in MCFast. . . . .	178
12.13	Distributions, produced by MCFast, of kinematic variables of secondary particles generated by an incident particle of 50 GeV/c: (a) $p_T$ distribution, (b) $\eta$ distribution . . . . .	178
12.14	Distribution of $p_t^2$ for elastic scattering from MCFast. . . . .	179
12.15	Hit pattern in a photon cluster in GEANT; The length of each line represents the energy in a single crystal. The simulation uses an internal energy cutoff to restrict the shower propagation. In this picture GEANT used a value of 100 keV. . . . .	185
12.16	Geometrical placement of cells in the parallel (left) and pointing (right) ECAL simulations. . . . .	186
12.17	Measured ratio of E9 over E25 versus simulated photon energy. . . . .	187
12.18	Second moment mass squared distribution for 40 GeV (left) and 70 GeV clusters (right). The simulated events contain either a single $\gamma$ or a single $\pi^0$ . Each contribution due to one of the particle species is normalized to 1. . . . .	188
12.19	Fraction of correctly found photons in the calorimeter. (a) versus simulated energy, at fixed radius (100 cm), (b) versus radius of impact point in ECAL, at fixed energy (10 GeV). See the text for the selection criteria. . . . .	190
12.20	(a) Distance of charged tracks to the closest reconstructed bump in the calorimeter for electrons/positrons (solid line) and for $\pi/K/p$ hadrons (dashed line); (b) $E/p$ for reconstructed charged tracks for electrons (solid line), all hadrons (dashed line), and hadrons with $E9/E25=1$ (dotted line); (c) $E9/E25$ shower shape variable for electrons (solid line) and hadrons (dashed line). . . . .	191
12.21	Electron identification efficiency as a function of track momentum in GeV/c for (a) electrons; and (b) hadrons. . . . .	192
13.1	Comparison of the number of found clusters in the BTeV calorimeter for single photons of 20 GeV; (a) GEANT with a 40 MeV cluster threshold, (b) GEANT with a 10 MeV cluster threshold, (c) MCFast with a 40 MeV cluster threshold. In each case, the primary cluster contains most of the energy. The secondary clusters are made from only one or two crystals, each containing a small amount of energy. . . . .	196

13.2	Comparison of the relative difference between the cluster energy and total energy from a 20 GeV single photon; (a) BTeVGeant reconstructed with a 40 MeV cluster threshold per crystal, (b) BTeVGeant with a 10 MeV cluster threshold per crystal, (c) MCFast with a 40 MeV cluster threshold per crystal	197
13.3	The difference between the photon energy and the reconstructed bump energies for 20 GeV photons as simulated by BTeVGeant. The bump energy is determined from the sum of crystal energies (a) E25 – summing 25 crystals around the peak; and (b) E49 – summing 49 crystals.	198
13.4	The difference between the photon energy and the reconstructed bump energies for 20 GeV photons as simulated by MCFast. The bump energy is determined from the sum of crystal energies (a) E25 for default MCFast; (b) E49 for default MCFast showers with 25 subhits per step in the transverse shower spread step; and (c) E49 for MCFast showers with 100 subhits per step.	198
13.5	Comparison of the hit pattern in a 20 GeV photon cluster as generated by (left) BTeVGeant, (right) MCFast. The length of each line represents the energy in a single crystal. Both plots use the same scale. The minimum energy per crystal is 40 MeV.	199
13.6	Comparison of number of crystals per cluster; (a) BTeVGeant reconstructed with a 40 MeV cluster threshold per crystal, (b) BTeVGeant with a 10 MeV cluster threshold per crystal, (c) and MCFast with a 40 MeV cluster threshold per crystal	200
13.7	Multiplicities of pixel hits and trigger primitives for events generated with BTeVGeant. See the text for details.	202
13.8	Multiplicities of pixel hits and trigger primitives for events generated with MCFast. See the text for details.	202
13.9	Comparison of straw chamber occupancies as computed by BTeVGeant (left) and MCFast (right). Station 2 (top) is the station which is second most downstream and station 7 (bottom) is the station which is closest to the interaction region. For all parts of the figure, the vertical axis the probability per beam crossing that the straw will have a hit.	203
13.10	Primary vertex multiplicity for $B^0 \rightarrow \pi^+\pi^-$ candidates which pass the analysis cuts described in Section 16.1.	204
13.11	Comparisons between MCFast and BTeVGeant using $B^0 \rightarrow \pi^+\pi^-$ candidates which pass the analysis cuts described in Section 16.1: a) the measured decay length minus the generated decay length, $\Delta L$ , for the $B^0$ candidate; b) $\Delta L/\sigma$ , where $\sigma$ is the error on $\Delta L$ ; c) the measured DCA minus the generated DCA, $\Delta_{DCA}$ , where DCA is the distance of closest approach of the $B^0$ candidate to the primary vertex; d) $\Delta_{DCA}/\sigma$ , where $\sigma$ is the error on $\Delta_{DCA}$ ; e) the measured $\pi^+\pi^-$ invariant mass; f) $\Delta M/\sigma$ , where $\Delta M$ is the measured $\pi^+\pi^-$ invariant mass minus the generated $B^0$ mass and where $\sigma$ is the error on $\Delta M$ . Each figure has about 1850 entries for BTeVGeant and about 2030 entries for MCFast.	205

14.1	a) the average number of pixel clusters per quadrant (solid line) for 31 tracking stations for minimum bias events with an average of two interactions per crossing. The dotted and dashed histograms show the number of pixel clusters in the inner and outer regions, respectively. Histograms in b) and c) show the average number of interior (dotted) and exterior (dashed) doublets and triplets per quadrant directed at one arm of the two-arm BTeV spectrometer, and d) shows the average number of tracks found for the same arm of the spectrometer. Histograms of doublets, triplets, and tracks directed at the other arm of the spectrometer are mirror images of histograms in b), c), and d). . . . .	210
14.2	Trigger response for minimum bias events with an average of two interactions per beam crossing. The figure shows four sets of points requiring at least 1, 2, 3, or 4 detached tracks. The arrows show a cut that requires at least 2 detached tracks with an impact parameter that exceeds $6\sigma$ , and achieves 99% rejection. . . . .	212
14.3	Trigger efficiency for $B_s \rightarrow D_s^+ K^-$ events with an average of two interactions per beam crossing. The figure shows four sets of points requiring at least 1, 2, 3, or 4 detached tracks. The arrows show a cut that requires at least 2 detached tracks with an impact parameter that exceeds $6\sigma$ , and gives a trigger efficiency of 74%. . . . .	214
14.4	Trigger efficiency for $B_s \rightarrow D_s^+ K^-$ vs. rejection for minimum bias events. The figure shows three sets of cuts requiring a minimum impact parameter for 2, 3, or 4 tracks. Increasing the impact parameter cut increases the fraction of minimum bias events that are rejected, and the arrows indicate the cut (2 tracks at $6\sigma$ ) that we use to achieve 99% rejection. . . . .	215
14.5	Fraction of $B_s \rightarrow D_s^+ K^-$ and minimum bias crossings, with an average of two interactions per crossing, that satisfy the Level 1 trigger for three different pixel efficiencies (three sets of points) vs. the number of noise hits that have been added to each pixel plane in the vertex detector. Results for minimum bias crossings have been multiplied by 10. . . . .	216
14.6	Distance between primary vertices . . . . .	217
14.7	Fraction of minimum bias crossings that satisfy the Level 1 trigger vs. the number of interactions per crossing. . . . .	218
14.8	The histogram of the detached $p_t$ sum, $\Sigma p_t $ , for two final states of interest and minimum bias events. The first bin corresponds to cases where no Level 2 detached track has been found. The probability for such occurrence (per crossing) is 32% for minimum bias and $\approx 15\%$ for $B$ events. . . . .	220
14.9	The efficiency of the Level 2 trigger vs. detached $P_t$ sum, $Pt_D$ , for two final states of interest and minimum bias events. The first bin corresponds to cases where no Level 2 detached tracks have been found. The probability for such occurrences (per crossing) is 32 % for minimum bias and $\approx 15\%$ for B events. . . . .	221

16.1	Distribution of signal (circles) and background (line) for the most important vertex and kinematic variables. (a) Normalized distance between primary and secondary vertex, $L/\sigma_L$ , (b) Normalized DCA of track with respect to the primary vertex, $DCA/\sigma_{DCA}$ (c) Transverse momentum of a track, (d) Maximum value of transverse momentum of two tracks, (e) $P_T$ imbalance of $\pi^+\pi^-$ with respect to the $B^0$ direction, and (f) $\chi^2$ of secondary vertex using the $\pi^+\pi^-$ with an additional track candidate. . . . .	233
16.2	Two body ( $\pi^+\pi^-$ ) mass plot without particle identification. Different decay channels are normalized by their production cross sections. The arrows indicate the range of the signal mass window. (Note the log scale.) . . . . .	234
16.3	RICH event selection: $\pi^+\pi^-$ signal efficiency vs contamination from other two-body decay modes . . . . .	234
16.4	Two body ( $\pi^+\pi^-$ ) mass plot with particle identification, normalized by their production cross sections. The arrows indicate the range of the signal mass window. (Note the log scale.) . . . . .	235
16.5	$\Delta P_T$ vs $P_T$ for pion tracks where $\Delta P_T$ is the difference between the generated and reconstructed $P_T$ . . . . .	236
16.6	Two body ( $K^+K^-$ ) mass plot without particle identification. Different decay channels are normalized by their production cross sections. The arrows indicate the range of the signal mass window. (Note the log scale.) . . . . .	238
16.7	Two body ( $K^+K^-$ ) mass plot with particle identification and normalized by their production cross sections. The arrows indicate the range of the signal mass window. . . . .	238
16.8	Distributions of $L/\sigma_L$ for (a) $J/\psi$ candidates from the decays of b-hadrons and (b) prompt $J/\psi$ candidates. The prompt candidates are suppressed by requiring $L/\sigma_L > 4$ . . . . .	241
16.9	The $J/\psi K_s^0$ invariant mass distribution for candidates which survive the selection criteria described in the text. . . . .	242
16.10	The $D^{*-}-D$ Q-value, $M(K^+\pi^-\pi^-) - M(K^+\pi^-) - 0.1455$ , in $\text{GeV}/c^2$ . . . . .	245
16.11	Four different sets of cuts on the $\gamma\text{-}\gamma$ mass spectrum: (upper left) $R_{min} < 7.5\text{ cm}$ and $E9/E25 < 0.85$ ; (upper right) $R_{min} < 10.0\text{ cm}$ and $E9/E25 < 0.85$ ; (lower left) $R_{min} < 15.0\text{ cm}$ and $E9/E25 < 0.85$ ; and (lower right) $R_{min} < 20.0\text{ cm}$ and $E9/E25 < 0.85$ . The fit is to a Gaussian and a fourth order polynomial. Most analysis work used the cuts of the plot in the upper right corner. . . . .	247
16.12	$P_t$ balance about the $B$ direction. . . . .	248
16.13	Resolution on $B$ polar angle, $\theta$ , measured from the fitted primary and $B$ vertices. The quantity plotted is $\theta_{measured} - \theta_{generated}$ . The width of the ‘‘core’’ of the distribution is about 1 milliradian. . . . .	249
16.14	Distribution of the $P_t$ balance variable for signal events. . . . .	249

16.15	Effect of $P_t$ balance cuts on signal events. Both histograms show the invariant mass of the $D^*\rho$ system. The solid histogram is before the $P_t$ balance cuts and the dashed histogram is after the cuts. The number of events is only slightly affected. . . . .	250
16.16	Effect of $P_t$ balance cuts on background events. Both histograms show the invariant mass of the $D^*\rho$ system. The solid histogram is before the $P_t$ balance cut and the dashed histogram is after the cuts. The number of events is reduced by a factor of more than 15. . . . .	250
16.17	$D^*\rho^+$ invariant mass for four values of the minimum allowed $\pi^0$ energy: (upper right) 2 GeV; (upper left) 3 GeV; (lower right) 4 GeV; and (lower left) 5 GeV. As the $\pi^0$ energy requirement is raised, the tails of the mass peak disappear. . . . .	252
16.18	The top left plot shows the number of interactions per crossing for this analysis. The next seven plots show the $D^* - \rho^+$ invariant mass plot when there are 1 to 7 interactions in the crossing. . . . .	254
16.19	Reconstructed mass plots for $\bar{B} \rightarrow D^{*+}\rho^-$ from CLEO. The data measured on the $\Upsilon(4S)$ are shown as points with error bars, the scaled continuum data are shown as filled rectangles and the estimated $B\bar{B}$ background in cross-hatch. The solid histogram is the result of the fit to a signal Gaussian and the two background components. The three plots are for different $D^0$ decay modes: (a) $K^-\pi^+$ , (b) $K^-\pi^+\pi^0$ and (c) $K^-\pi^+\pi^+\pi^-$ . . . . .	255
16.20	$L/\sigma_L$ and mass peaks for $B_s$ and $D_s$ . . . . .	260
16.21	Proper time resolution for $B_s$ : $t_{gen} - t_{rec}$ (nsec). . . . .	260
16.22	Comparison of $B_s \rightarrow D_s K$ signal and background from $B_s \rightarrow D_s X$ , where X contains at least one pion misidentified as a $K$ . . . . .	262
16.23	Fitted values of $\gamma$ , $\delta$ , and $\Delta\Gamma$ . . . . .	264
16.24	Invariant mass of $B^- \rightarrow \bar{D}^0 K^-$ . . . . .	268
16.25	Signal (solid line) and background (dashed line) from $B^- \rightarrow \pi^- D^0$ and $B^- \rightarrow \pi^- D^0 X$ where the $\pi^-$ is misidentified as a $K^-$ . . . . .	270
16.26	Calculated values of $\gamma$ and $b$ for input values $\gamma = 65^\circ(1.13 \text{ rad})$ , $b = 2.2 \times 10^{-6}$ . . . . .	271
16.27	$K_s\pi$ mass . . . . .	274
16.28	Invariant $\pi^+\pi^-\pi^0$ mass distributions for background (left) and signal (right) events for $B \rightarrow \rho^0\pi^0$ . . . . .	277
16.29	Invariant $\pi^+\pi^-\pi^0$ mass distributions for background (left) and signal (right) events for $B \rightarrow \rho^+\pi^-$ . . . . .	277
16.30	The invariant mass distributions for (a) $\eta \rightarrow \gamma\gamma$ , (b) $\eta' \rightarrow \pi^+\pi^-\gamma$ , and $\eta' \rightarrow \pi^+\pi^-\eta$ , $\eta \rightarrow \gamma\gamma$ . The Gaussian mass resolutions are indicated. . . . .	281
16.31	(a) The dimuon invariant mass. (b) The reconstructed $B_s$ mass for all three final states of $\eta$ and $\eta'$ summed together. The solid curve is the done with without constraining the the $\mu^+\mu^-$ to the $J/\psi$ mass, while the dashed curve is done using the constraint. The $B_s$ mass resolution improves from 19 to 11 MeV/c <sup>2</sup> . . . . .	282

16.32	Distributions of backgrounds in several variables compared with signal. For $\eta' \rightarrow \rho\gamma$ (a) $DCA/\sigma_{DCA}$ , (b) $\chi^2$ of adding an additional track to the $J/\psi\pi^+\pi^-$ vertex; for $\eta \rightarrow \gamma\gamma$ (c) energy of the photons and (d) the transverse momentum of the photons with respect to the beam direction. The arrows show the position of the cuts. . . . .	283
16.33	Mini-Monte Carlo proper lifetime plots of a) unmixed and b) mixed decays for a generated value of $x_s = 40$ . The plots simulate the results of the $B_s \rightarrow D_s^- \pi^+$ channel after one month of running. The oscillations are prominent. Part c) shows the negative log likelihood function which was obtained from the entries in parts a) and b). A prominent minimum is seen at the generated value of $x_s$ . The dashed line marks the level above the minimum which corresponds to $5\sigma$ significance. . . . .	290
16.34	The same likelihood function as in part c) of the previous figure but obtained using the integral method described in the text. The overall shape is the same but the statistical fluctuations have been removed. There is also an overall level shift which is related to the goodness of fit in the previous figure. . . .	291
16.35	The $x_s$ reach of the BTeV detector. The curves indicate the number of years of running which are required to make a measurement of $x_s$ with a statistical significance of $5\sigma$ ; a safety margin, discussed in the text, has been included in the definition of $5\sigma$ . The curves are for the two different decay modes indicated on the figure. . . . .	292
16.36	Forward-backward asymmetry in the Standard Model (left) [25]. Predictions of the SUGRA (MIA-SUSY) model [26], with various values of the Wilson coefficients (right). . . . .	294
16.37	Distributions of cut variables for signal (points) and $b\bar{b}$ background (hatched) MCFast events. . . . .	296
16.38	Distributions of tagged $B^0 \rightarrow K^{*0}\mu^+\mu^-$ signal (left) and $4.4\text{ fb}^{-1}$ of $b\bar{b}$ background (right) MCFAST events. . . . .	297
16.39	Expected forward-backward asymmetry distribution, including background, (left) and number of events (not including background) (right) as a function of $m(\mu^+\mu^-)$ after one year of running. . . . .	298
16.40	Distributions of $B^+ \rightarrow K^+\mu^+\mu^-$ signal (left) and $10\text{ fb}^{-1}$ of $b\bar{b}$ background (right) events. . . . .	300
16.41	$B$ mass distributions of $B^{+0} \rightarrow K^+n(\pi^{+/-})\mu^+\mu^-$ ( $n = 0-4$ ) from $100\text{ pb}^{-1}$ of tagged signal (left) and anti-tagged combinatoric background (center) events. $B$ mass distribution of $0.24\text{ pb}^{-1}$ of $b\bar{b}$ background Monte Carlo events (right), where both $b$ 's decay semileptonically. . . . .	302
16.42	The Level 1 trigger efficiency for $B_s \rightarrow D_s^+K^-$ and minimum bias events (multiplied by 10 for better viewing) for three values of assumed pixel efficiencies as a function of the number of added noise hits per plane. We expect, nominally, 5 noise hits per plane, corresponding to a density of $10^{-5}$ noise hits.	304



16.43	The efficiency for identifying both pions in the reaction $B^0 \rightarrow \pi^+\pi^-$ versus the efficiency for misidentifying $B^0 \rightarrow K^+\pi^-$ as $\pi^+\pi^-$ . The solid-line is for the baseline design, while the dashed line is for a 50% loss of photons. . . . .	305
A.1	Spatial distribution of the particle fluence in a pixel plane. . . . .	334
A.2	SINTEF wafer from joint BTeV/CMS submission. . . . .	335
A.3	$I-V$ characterization of two different sensor cells on a SINTEF wafer recently received at Fermilab. . . . .	336
A.4	Collected charge spreading in a 300 $\mu\text{m}$ silicon detector a) produced by diffusion, b) produced by the interplay of diffusion and the magnetic field for $B=1.6\text{T}$ , and c) produced by diffusion and magnetic field effects when the charged track is incident at an angle of 100 mr in the bend plane. . . . .	338
A.5	The reconstructed x coordinate as a function of the charged track impact point on the pixel cell in a 1.6 T magnetic field, for a pixel size of $50 \times 400 \mu\text{m}^2$ , and normal incidence. Both these coordinates are measured with respect to the pixel center. . . . .	339
A.6	The reconstructed x coordinate as a function of the charged track impact point on the pixel cell in a 1.6 T magnetic field, for a pixel size of $50 \times 400 \mu\text{m}^2$ , and incidence angle in the bend plane $\theta_X = 300$ mr. Both these coordinates are measured with respect to the pixel center. . . . .	340
A.7	a) Spatial resolution in the reconstructed x coordinate as a function of the threshold for a pixel size of $50 \times 400 \mu\text{m}^2$ and incidence angle in the bend plane $\theta_X = 300$ mr. b) percentage of events having N pixels hit as a function of the threshold for the same configuration. . . . .	341
A.8	Number of pixels hit for a 50 $\mu\text{m}$ pixel small dimension as a function of the track orientation. The magnetic field is parallel to the $\hat{x}$ direction. . . . .	341
A.9	Resolution for binary readout and 4-bit ADC readout for 50 $\mu\text{m}$ pixel small dimension. The magnetic field is parallel to the $\hat{x}$ direction. . . . .	342
A.10	Number of pixels hit per crossing in the hottest pixel readout chip (nearest to the beam). The upper histogram shows the occupancy expected at a luminosity of $2 \times 10^{32} \text{cm}^{-2} \text{sec}^{-1}$ . The lower histogram shows the occupancy expected in $b$ events at this luminosity. . . . .	343
A.11	Schematic drawing of the silicon telescope. . . . .	346
A.12	Calibration for the FPIX0 p-spray (CiS) sensor. Plot a) shows a Tb x-ray spectrum. The arrow indicates the $K_\alpha$ peak. Plot b) shows the pulser calibration data for all channels, and plot c) shows a discriminator threshold curve for a single channel. Curves like the one shown in c) are used to determine the amplifier noise and discriminator threshold dispersion. . . . .	347
A.13	The plot on the left shows the “improved Landau” fit of the pulse height distribution for the CiS p-spray sensor bump-bonded to an FPIX0 chip, when the track is at normal incidence. The plot on the right shows the average charge collected as a function of track position. . . . .	350

A.14	The plot on the left shows the “improved Landau” fit of the pulse height distribution for the CiS p-stop sensor bump-bonded to an FPIX0 chip, when the track is at normal incidence. The plot on the right shows the distribution of tracks that leave a signal less than 15000 e <sup>-</sup> in the detector. . . . .	350
A.15	The plot on the left shows the fraction of the time that the indicated cluster size was recorded as a function of detector bias for a fixed readout threshold and a variety of angles. The plot on the right shows the same fraction as a function of the detector readout threshold for a fixed bias voltage and a variety of angles. These data were recorded by the p-stop FPIX0 detector, which has a depletion voltage of ~-85V. . . . .	351
A.16	The histogram on the left is the $\eta$ distribution for data collected with beam normally incident on the FPIX0 p-stop sensor. An entry is made in this histogram only if exactly two adjacent pixels in a single column are hit. The plot on the right shows the difference between the predicted track X-position and the position of the edge between the two hit pixels, as a function of $\eta$ for the same data. . . . .	352
A.17	Residual distributions for the FPIX0 p-stop detector. $\sigma_G$ is the standard deviation of the Gaussian fit to each residual plot. . . . .	353
A.18	Position resolution as a function of beam incidence angle for the FPIX0-instrumented CiS p-stop sensor. The curves are the simulated RMS for $Q_{thres} = 2500 e^-$ . The oscillating curve is the simulated digital resolution; the lower curve assumes 8-bit charge digitization. The squares are the Gaussian $\sigma$ 's shown in Figure A.17, and the triangles are the $\sigma$ 's extracted from fits to residual distributions made without using charge sharing information. . . . .	354
A.19	Position resolution as a function of beam incidence angle for an FPIX1-instrumented Seiko p-stop sensor. The curve is the simulated RMS for $Q_{thres}=3780 e^-$ , assuming 2-bit charge digitization. The squares are $\sigma$ 's from Gaussian fits to the residual distributions. . . . .	355
A.20	Spatial resolution versus bias voltage for readout threshold and track angle fixed (left plot). Spatial resolution versus readout threshold for bias voltage and track angle fixed (right plot). The data are from FPIX0 p-stop. . . . .	356
A.21	Residual distributions of FPIX0 p-spray detector at zero degrees fitted with the functions described in this chapter. The plot on the left shows the distribution for cluster size 1 and the plot on the right for clusters having more than one hit. . . . .	357
A.22	Residual distributions for the FPIX0 p-stop detector. The data are the same as shown in Figure A.17, plotted here using a log scale to make the tails of the distributions easier to see. The curves superimposed on the plots are the resolution functions which were used in Monte Carlo studies of the BTeV trigger. . . . .	358
A.23	Block diagram of the analog cell in VA circuits. . . . .	363

A.24 Aerogel Transmittance as a function of wavelength, for six Matsushita samples. Points represent the data, the line represents a fit made to the standard Hunt formula. . . . .	368
A.25 Aerogel Transmittance as a function of wavelength, for samples from different sources. The data points indicate the mean transmittance of the Matsushita samples, whereas the lines are Hunt parameter fits as described in the text, all normalized to 1 cm thickness. . . . .	369
A.26 Aerogel Transmittance as a function of wavelength, for a stack of 4 Matsushita tiles (data points), and for the Matsushita samples extrapolated to 4 cm bulk thickness (thick line). Other samples are shown for comparison. . . . .	370
A.27 Two views of the lens system proposed by R. Forty for use with closely packed arrays of Hamamatsu R5900 MAPMTs. The pictures are taken from Ref.[18].	372
A.28 Annual radiation dose in crystals at shower maximum. Note that a yearly dose of 1 kGy corresponds to a dose rate of 0.3 Gy/hour. . . . .	377
A.29 Annual radiation dose at PMT windows. . . . .	378
A.30 Energy resolution as a function of incident photon energy for 220 mm long crystals and 5x5 clustering. . . . .	379
A.31 Distribution of measured photon energies for 10-GeV photons using a realistic clustering algorithm. The curve shows the result of a fit to a resolution function.	380
A.32 Energy-dependent energy resolution. The curve shows the result of a fit to a resolution function. . . . .	381
A.33 Measured photon position $x_{C1}$ versus known photon position $x_0$ for 30 GeV photons. . . . .	382
A.34 Distribution of $\Delta x = x_{\text{corr}} - x_0$ for 30 GeV photons. The fit is a Gaussian with mean consistent with zero and $\sigma = 0.7$ mm. . . . .	383
A.35 Energy-dependent position resolution. The curve shows the result of a fit to resolution function. . . . .	384
A.36 Energy deposited for 80 GeV/c photons normally incident on PbWO <sub>4</sub> crystals of the labeled lengths. . . . .	385
A.37 Fit of the normalized clustered energy deposit for normally incident 20 GeV photons in crystals of length 210 mm. The fitted line shape is from the Crystal Ball experiment. . . . .	386
A.38 Energy resolution as a function of incident photon energy for different crystal lengths using 5x5 clustering. The squares are for a crystal length of 230 mm, the triangles for 220 mm and the inverted triangles for 210 mm. . . . .	387
A.39 Two-photon invariant mass distributions for simulated $\pi^0$ 's of energy 5, 10 and 30 GeV. . . . .	388
A.40 Cluster mass distribution for $\gamma$ 's and $\pi^0$ 's obtained with a full BTeVGeant simulation. Energy of the photons and $\pi^0$ 's is 40 GeV, 60 GeV and 70 GeV, as indicated. . . . .	393

A.41	$\gamma\gamma$ mass distribution for events containing a $B$ event as well as a few minimum-bias events. The energy of the $\pi^0$ candidates are required to be greater than 10 GeV (top) and 5 GeV (bottom), respectively. . . . .	394
A.42	End and top views of one “plank” of proportional tubes. . . . .	397
A.43	(left) Beams-eye view of one muon detector station, which consists of eight overlapping octants arranged in two layers. One octant is cut away in places to show the overlap between adjacent octants. (right) Arrangement of planks to form the four views in an octant ( $r$ view is repeated). There will be 13 planks per view (more than shown). . . . .	398
A.44	Photo of the muon testbeam setup. The beam direction was from right to left. Three of the one-foot planks and the two six-foot planks can be seen. The remaining planks (two three-foot planks and three more one-foot planks) are further back. The planks and cables are wrapped in aluminum foil to provide shielding. The amplifiers are inside boxes made of copper-plated G10. . . . .	403
A.45	Plateau curves (efficiency versus voltage) for a one-foot, three-foot, and six-foot plank of tubes. We require hits in scintillators upstream and downstream of the muon planks and for these events we read out single-hit LeCroy TDC’s to determine if a hit occurred at the proper time. The drop in efficiency above the plateau is due to the particular readout electronics (single-hit TDC’s with a long gate) when high hit rates are encountered. These data were taken using the tubes strung with 30 micron wire with 80%/20% Ar/CO <sub>2</sub> gas. . . . .	404

# List of Tables

1.1	Resulting decay amplitudes from the fit to the transversity angles. The first error is statistical and the second is the estimated systematic uncertainty. . .	15
1.2	$B^0 \rightarrow \rho\pi$ Decay Modes . . . . .	18
1.3	Amplitudes and Phases for $B^- \rightarrow D^0/\bar{D}^0 K^-$ . . . . .	22
1.4	Time evolution of the decay $B_s \rightarrow J/\psi(\rightarrow l^+l^-)\phi(\rightarrow K^+K^-)$ of an initially (i.e. at $t = 0$ ) pure $B_s$ meson. $\delta_{1,2}$ are strong phase shifts. . . . .	28
1.5	Primary modes useful for measuring CP asymmetries for different CKM angles	30
1.6	Other modes useful for cross-checking $\sin(2\beta)$ . . . . .	31
1.7	Experimental results for $b \rightarrow s\gamma$ . . . . .	34
1.8	Searches for $b \rightarrow s\ell^+\ell^-$ decays . . . . .	36
1.9	Upper limits on $b \rightarrow$ dilepton decays (@90% c.l.) . . . . .	37
2.1	The Tevatron as a $b$ and $c$ source for BTeV . . . . .	51
3.1	BTeV/C0 Vertex Dipole Properties . . . . .	56
4.1	Pixel Vertex Detector . . . . .	63
4.2	Material budget of a BTeV pixel plane. The column labelled “coverage” shows the factor applied to account for overlaps of the sensors and readout chips, and for geometric coverage (e.g. area covered by bump bonds/total area). The numbers given for components on the HDI and for glue are derived from the ATLAS Pixel Detector TDR [5]. . . . .	67
5.1	Properties of the baseline forward straw tracker . . . . .	73
5.2	Properties of the baseline forward silicon tracker . . . . .	73
5.3	Summary of material specifications for the BTeV prototype straw tubes . . .	75
6.1	Expected performance of BTeV RICH system. The photon yield and the resolution per track given here do not take into account any reconstruction losses due to overlap of Cherenkov rings from different tracks in the same event. . . . .	90
7.1	Properties of $\text{PbWO}_4$ . . . . .	94
7.2	Properties of the BTeV electromagnetic Calorimeter . . . . .	95

8.1	Parameters of the baseline BTeV Muon System. . . . .	106
9.1	DSP processing times and numbers of DSPs required for the track- and vertex-processing farms. The numbers of DSPs are based on the time required to complete the track and vertex calculations in 132ns, on average. . . . .	127
9.2	Level 1 trigger efficiencies for minimum-bias events and various processes of interest that are required to pass off-line analysis cuts. All trigger efficiencies are determined for the Level 1 vertex trigger for beam crossings with an average of two interactions per crossing using the Monte Carlo code shown in the table. . . . .	130
10.1	Estimates of Hardware for BTeV Trigger and Data Acquisition System . . .	136
12.1	Summary of BTeVGeant simulations run on the Fermilab PC Farm. The data output sizes shown are for the compressed output. . . . .	172
13.1	Results obtained by fitting each histogram in Figure 13.11 to a Gaussian. The fits were performed over an interval of approximately $\pm 3\sigma$ about the mean. .	206
14.1	Level-1 trigger efficiencies for minimum-bias events and various processes of interest that are required to pass off-line analysis cuts. All trigger efficiencies are determined for beam crossings with an average of two interactions per crossing using the Monte Carlo code shown in the table. . . . .	213
14.2	The average multiplicity of Level 2 detached tracks $\langle N_{sec} \rangle$ from various sources in events passing the analysis cuts and the Level 1 + Level 2 trigger. A noise track is a track not coming from either a primary vertex or from a heavy quark or strange decay (e.g. secondary interactions). Also listed are the probability $P_{>=1}$ ( $P_{>=2}$ ) to find at least one (two) of these tracks in the sample of Level 2 detached tracks. . . . .	222
15.1	Results, to date, of first generation studies of tagging power. In the text it is discussed that these studies are incomplete and that they likely underestimate the tagging power which can be realized at BTeV. . . . .	229
16.1	Projected yield of $B^0 \rightarrow \pi^+ \pi^-$ and the uncertainty on $a_{CP}$ from the BTeVGeant simulation. . . . .	237
16.2	Projected yield of $B_s \rightarrow K^+ K^-$ and fake rates. . . . .	239
16.3	Summary of the sensitivity to $\sin(2\beta)$ using $B \rightarrow J/\psi K_s^0$ . The time dependent method provides the better sensitivity. . . . .	243
16.4	Details of the calculation of the signal and background events obtained in one year of running for the decay $B^0 \rightarrow D^{*-} \rho^+$ . . . . .	253
16.5	CLEO yields for $\overline{B} \rightarrow D^{*+} \rho^-$ . . . . .	255
16.6	Projected Number of Reconstructed $B_s^0 \rightarrow D_s K$ per year . . . . .	259
16.7	RICH efficiency. . . . .	263

16.8	Results of fits with variation of input parameters. . . . .	265
16.9	Cuts for $D^0 \rightarrow K\pi$ and $D^0 \rightarrow K^+K^-$ . . . . .	268
16.10	Projected number of reconstructed $B^- \rightarrow K^-D$ per year. . . . .	269
16.11	Input values of parameters and results of fit for $\gamma$ . . . . .	270
16.12	Selection Criteria . . . . .	276
16.13	$B \rightarrow \rho\pi$ Yields . . . . .	278
16.14	Relevant branching fractions. . . . .	279
16.15	Projected yield of $B_s \rightarrow J/\psi\eta'$ ( $B_s \rightarrow J/\psi\eta$ ) and the uncertainty on $\chi$ . . . . .	284
16.16	Projected yield for $B_s \rightarrow D_s^- \pi^+$ in one year of BTeV running. The numbers in the third column give the expected yield when all of the factors down to and including that line have been considered. The branching fraction $\mathcal{B}(B_s \rightarrow D_s^- \pi^+)$ was estimated to be the same as $\mathcal{B}(B_d \rightarrow D^- \pi^+)$ . The value for $\mathcal{B}(\bar{b} \rightarrow B_s)$ was obtained from [3]. . . . .	287
16.17	Projected yield for $B_s \rightarrow J/\psi\bar{K}^{*0}$ in one year of BTeV running. The numbers in the third column give the expected yield when all of the factors down to and including that line have been considered. The estimate for $\mathcal{B}(B_s \rightarrow J/\psi\bar{K}^{*0})$ was obtained from [21] and that for $\mathcal{B}(\bar{b} \rightarrow B_s)$ was obtained from [3]. The trigger efficiency is quoted as a fraction of those events which pass the analysis cuts. . . . .	288
16.18	Estimated branching fractions and current measurements of flavor-changing neutral current decays with muons and electrons. . . . .	293
16.19	Estimate of sensitivity to $B^0 \rightarrow K^{*0}\mu^+\mu^-$ based on one year of running. Only backgrounds from $b\bar{b}$ semileptonic decays were included in this study. . . . .	298
16.20	Estimate of sensitivity to $B^+ \rightarrow K^+\mu^+\mu^-$ based on one year of running. . . . .	300
16.21	Estimate of sensitivity to $(B_d, B_u) \rightarrow X_s\mu^+\mu^-$ based on one year of running. . . . .	302
17.1	Yearly sensitivities for CP violating quantities. . . . .	309
17.2	Number of tagged $B^0 \rightarrow \pi^+\pi^-$ ( $\mathcal{B}=0.43 \times 10^{-5}$ ). . . . .	312
17.3	Number of $B^- \rightarrow \bar{D}^0 K^-$ ( $\mathcal{B}=1.7 \times 10^{-7}$ ). . . . .	312
17.4	Event yields and signal/background for $B^0 \rightarrow \rho\pi$ . . . . .	314
17.5	Comparison of BTeV and LHC-b sensitivities for $B_s \rightarrow D_s^\pm K^\mp$ . . . . .	316
18.1	Baseline BTeV Detector Cost Estimate (\$) . . . . .	329
18.2	Preliminary BTeV computing cost estimate (\$) . . . . .	330
A.1	Cluster size fraction for various angles of incidence for FPIX0 p-stop regular gain cells. For each angle, the sample size is about 20000 tracks. These data were collected with a sensor bias voltage of -140 V, and a discriminator threshold of 2500 e <sup>-</sup> . . . . .	351
A.2	Reconstructed $\pi^0$ mass resolution. . . . .	389
A.3	Photon detection efficiencies for 99% $\pi^0$ rejection . . . . .	389
A.4	Operating parameters for different gasses and inner wire radii (a). The values of $t_{drift}^M$ assume a wire space of 0.5 cm. . . . .	401